

## Fluorescent polymers for environmental monitoring: Targeting pathogens and metal contaminants with naphthalimide derivatives

Joana Galhano <sup>a</sup>, Atanas Kurutos <sup>b,c,\*</sup>, Georgi M. Dobrikov <sup>b</sup>, Maria Paula Duarte <sup>d</sup>, Hugo M. Santos <sup>e</sup>, Jose Luis Capelo-Martínez <sup>e</sup>, Carlos Lodeiro <sup>e,\*\*</sup>, Elisabete Oliveira <sup>e,\*\*</sup>

<sup>a</sup> BIOSCOPE Research Group, LAQV-REQUIMTE, Chemistry Department, NOVA School of Science and Technology, Universidade NOVA de Lisboa, Caparica 2829-516, Portugal

<sup>b</sup> Institute of Organic Chemistry with Centre of Phytochemistry, Bulgarian Academy of Sciences, Acad. G. Bonchev str., bl. 9, Sofia 1113, Bulgaria

<sup>c</sup> University of Chemical Technology and Metallurgy, 8 St. Kliment Ohridski Blvd, Sofia 1756, Bulgaria

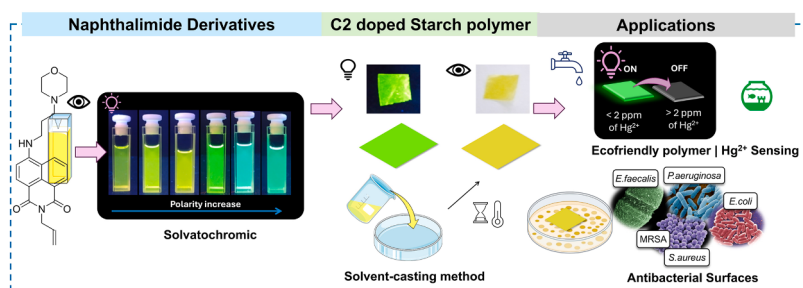
<sup>d</sup> METRICS / NOVA School of Science and Technology, Universidade NOVA de Lisboa, Campus de Caparica, Caparica 2829-516, Portugal

<sup>e</sup> PROTEOMASS Scientific Society, Costa da Caparica 2825-466, Portugal

### HIGHLIGHTS

- Three new naphthalimides show dual antibacterial and heavy metal sensing functions.
- Naphthalimides were integrated into PVC, PMMMA, and Starch polymeric matrixes.
- C2-starch polymers detect  $\text{Hg}^{2+}$  down to 3 nM spectroscopically, 4  $\mu\text{M}$  visually.
- Starch biopolymers synthesized via a green, sustainable, and non-toxic method.

### GRAPHICAL ABSTRACT



### ARTICLE INFO

**Keywords:**  
 Naphthalimide-based compounds  
 $\text{Hg}^{2+}$  detection  
 Antibacterial dye-doped polymers  
 Starch biopolymer  
 Ecotoxicity-free  
 On-site evaluation

### ABSTRACT

Monitoring  $\text{Hg}^{2+}$  levels in aqueous environments is crucial to assess the potential methylmercury contamination via bacterial conversion, however, existing methods often require extensive sample treatment and expensive equipment. To mitigate this issue, this study examines the synthesis and application of three naphthalimide-based compounds, with significant fluorescent and solvatochromic behavior (C1, C2, and C3). Compounds C1 and C2 demonstrated a strong affinity for  $\text{Hg}^{2+}$  metal ions, with C2 showing selectivity and a strong antibacterial profile, particularly against *S. aureus* ( $\text{MIC}_{50}$  (C2) = 0.01  $\mu\text{g}/\text{mL}$ ). Moreover, these compounds were incorporated into three polymeric matrices, namely polyvinyl chloride (PVC), poly (methyl methacrylate-co-methacrylic acid) (PMMMA), and Starch, allowing for the development of solid-support sensors/surfaces with a strong antibacterial profile, highlighting the inherent dual-functionality of the compounds. Interestingly, the C2-doped Starch biopolymer detected low concentrations of  $\text{Hg}^{2+}$  ions, such as 23 nM in tap water (value within the WHO standards for drinking water), through a rapid spectroscopic evaluation without sample treatment. This biopolymer was generated via a sustainable, green-chemistry-oriented, temperature-dependent water/Starch

\* Corresponding author at: Institute of Organic Chemistry with Centre of Phytochemistry, Bulgarian Academy of Sciences, Acad. G. Bonchev str., bl. 9, Sofia 1113, Bulgaria.

\*\* Corresponding authors.

E-mail addresses: [Atanas.Kurutos@orgchm.bas.bg](mailto:Atanas.Kurutos@orgchm.bas.bg) (A. Kurutos), [cle@fct.unl.pt](mailto:cle@fct.unl.pt) (C. Lodeiro), [ej.oliveira@fct.unl.pt](mailto:ej.oliveira@fct.unl.pt) (E. Oliveira).

synthetic route, without the addition of plasticizers and any associated ecotoxicity. The study used sustainable methods for environmental monitoring and antibacterial applications, advancing material science to offer effective, accessible, and eco-friendly solutions for detecting and mitigating mercury pollution and bacterial contaminations, enhancing environmental and health safety.

## 1. Introduction

The development of colorimetric and fluorometric sensors to detect hazardous substances is rapidly advancing, with numerous studies highlighting their significance [1,2]. These probes offer simple, fast, and sensitive strategies to address environmental pollution issues through simple detection mechanisms.

Among all known pollutants, heavy metal contamination of aqueous environments is a major environmental concern, as indicated by the U.S. Environmental Protection Agency (EPA) [3]. This type of contamination can arise from various industrial and urban activities [4]. Amongst heavy metals, mercury is one of the most dangerous pollutant agents, listed in the World Health Organization's (WHO) top 10 chemicals of public health concern [5]. Its presence in aqueous environments derives mainly from industrial processes such as pharmaceutical production. Due to a greater understanding of mercury's toxic and nefarious effects on human health, there is a growing need to develop materials for its detection [6]. Inorganic mercury, particularly  $Hg^{2+}$ , is the predominant form found in aqueous environments and can have harmful effects on human health [7]. Moreover,  $Hg^{2+}$  can be bio-transformed into methylmercury through a bacteria-mediated process. Monitoring  $Hg^{2+}$  levels is crucial as it is a potential indicator of methylmercury contamination in aqueous environments.

Traditional methods for mercury detection in aqueous environments, include atomic absorption spectrometry or inductively coupled plasma mass spectrometry (ICP-MS), which are considered highly efficient and accurate. However, several disadvantages arise, especially the utilization of expensive equipment, complex and time-consuming sample treatment procedures, and specialized training. In contrast, colorimetric or fluorometric-based methods can minimize such disadvantages, providing faster results through simpler experimental protocols. The simplicity of these assays is not hindered by the existence of low detection limits, with some reports reaching concentrations of 0.38 nM [8–13].

Naphthalimides, a class of aromatic heterocycles, are known for their impressive photophysical properties. They exhibit intense fluorescence intensity in the UV-Vis regions, high fluorescence quantum yields, and long-lived excited states [14]. This makes them ideal chromophores for developing probes, particularly for  $Hg^{2+}$  detection. Several literature studies employed naphthalimide-based probes for  $Hg^{2+}$  detection in various environments, from biological samples to organic solvents [15–17]. Additionally, the photophysical characteristics of naphthalimides can be effectively modified through the functionalization of the aromatic naphthalene moiety and the 'N-imide site' [18]. Specific alterations can tailor absorption and fluorescence properties, allowing for various applications as dyes or bioactive compounds, among others [19–29]. This increased bioactivity originates from the DNA-binding mechanisms derived from the tricyclic planar ring configuration of the naphthalimide scaffold [19].

Incorporating naphthalimides into solid-support platforms can produce interesting multifunctional materials, such as effective heavy metal sensors with inherent bioactive properties. This combination yields a more durable material for environmental and clinical applications requiring fewer maintenance procedures [30].

Selecting the appropriate polymeric matrix ensures the production of a homogeneous material and prevents aggregation or phase separation phenomena. Polyvinyl chloride (PVC) and poly (methyl methacrylate-co-methacrylic acid) (PMMMA) are among the most used plastics nowadays. They are traditionally derived from petrochemical sources

and are now being re-envisioned through "green chemistry" approaches to enhance sustainability in production [31–33]. Bio-based polymers, such as Starch polymers, are good candidates for this application due to their production processes being based on green chemistry processes and are typically produced in aqueous environments under mild conditions [34].

Previous studies have independently explored the photophysical properties of naphthalimides and the use of various polymers for environmental sensing or antibacterial purposes. However, this work uniquely integrates these elements into multifunctional smart materials. The application of PVC, PMMMA and Starch as solid-support matrices and doping with three naphthalimide derivates (C1, C2, and C3) allowed the development of polymers that sensitively detect low mercury concentrations in aquatic environments and exhibit strong antibacterial properties against resistant bacterial strains. Additionally, our study introduces a novel aqueous-based method for Starch polymer production, emphasizing sustainability and reproducibility, while ensuring the non-toxic nature of the polymers. These polymers allow for easy mercury detection in aqueous environments and exhibit inhibitory bacterial behavior against Gram-positive and Gram-negative bacteria. This versatile Starch-based platform has the potential to incorporate diverse organic molecules, without any inherent associated ecotoxicity (MICROTOX@Assay), facilitating the production of sustainable polymers applicable in environmental and clinical settings.

## 2. Experimental

### 2.1. Chemicals and starting materials

4-Bromo-1,8-naphthalic anhydride (95 %), N,N-Dimethylformamide (anhydrous, 99.8 %), 2-Picolylamine (99 %), Magnesium sulfate (puriss. p.a., drying agent, anhydrous, ≥98.0 %), and 2-Mercaptoethanol (≥99.0 %) were purchased from Sigma-Aldrich. Allylamine (>99.0 %), and N-(3-Aminopropyl)morpholine (>99.0 %) were purchased from Tokyo Chemical Industry Co. Ltd. Potassium carbonate (anhydrous 99.0 %) was purchased from Fluorochem Ltd. Triethylamine (99 %) was purchased from Acros Organics. Silica gel (high-purity grade, pore size 60 Å, 230–400 mesh particle size, 40–63 µm particle size, for flash chromatography) employed for the column chromatography was purchased from Sigma Aldrich. Copper (II) trifluoromethanesulfonate Cu(TfO)<sub>2</sub>, > 98 %, Cadmium (II) trifluoromethanesulfonate Cd(TfO)<sub>2</sub>, > 98 %, Mercury (II) trifluoromethanesulfonate Hg(TfO)<sub>2</sub>, > 98 %, Nickel (II) trifluoromethanesulfonate Ni(TfO)<sub>2</sub>, > 98 %, Cobalt (II) trifluoromethanesulfonate Co(TfO)<sub>2</sub>, > 98 %, Zinc (II) trifluoromethanesulfonate Zn(TfO)<sub>2</sub>, > 98 % and Silver (I) trifluoromethanesulfonate AgTfO, > 98 %, were acquired from Solvachem. Chromium (III) nitrate nonahydrate Cr(NO<sub>3</sub>)<sub>3</sub>·9 H<sub>2</sub>O > 99 %, Iron (III) nitrate nonahydrate Fe(NO<sub>3</sub>)<sub>3</sub>·9 H<sub>2</sub>O 98–101 %, Iron(II) sulfate heptahydrate FeSO<sub>4</sub>·7H<sub>2</sub>O > 99 % and Aluminium Nitrate Nonahydrate Al(NO<sub>3</sub>)<sub>3</sub>·9 H<sub>2</sub>O > 98 % were acquired from Sigma Aldrich.

Deuterated DMSO-d<sub>6</sub> (99.80 %) and chloroform-d (99.80 %) were acquired from Deutero GmbH. Absolute ethanol (EtOH) was acquired from Carlo Erba Reagents. Dimethyl sulfoxide (DMSO), Tetrahydrofuran (THF), Chloroform, Acetonitrile (ACN), Toluene, Polyvinyl chloride (PVC), Poly (methyl methacrylate-co-methacrylic acid) (PMMMA), Starch, and Sodium Chloride (NaCl) were purchased from Sigma Aldrich. Tryptone Soy Agar (TSA), Mueller-Hinton Agar (MHA) and Mueller-Hinton Broth (MHB) were purchased from Biokar. Acute Reagent and Reconstitution Solution were purchased from ModernWater.

All solvents and reagents were of analytical reagent grade and were used as received.

## 2.2. Instrumentation

Absorption spectral acquisition was performed in a JASCO V-650 Spectrophotometer. Solid state and liquid fluorescence emission spectra were acquired using a HORIBA-Jobin-Yvon Fluoromax-4® spectrofluorometer. For the acquisition of solid-state spectra, an optic fiber attached to the spectrofluorometer was required. Lifetime measurements were conducted in a TEMPRO Fluorescence Lifetime System with a Nanoled pulsed diode controller from HORIBA-Jobin-Yvon. For the measurements of 96-well plates, a CLARIOSTAR spectrophotometer (BMG Labtech) was used. Infrared spectra (FTIR-ATR) were acquired on a FTIR spectrophotometer Bruker Tensor 27. Data acquisition was performed with a resolution of  $2\text{ cm}^{-1}$  using an ATR appliance – Pike Miracle with ZnSe Crystal Plate. All previous equipment was available from the PROTEOMASS Scientific Society-BIOSCOPE Facility.

Differential Scanning Calorimetry (DSC) was performed in a DSC131, Setaram, France, and Thermogravimetric Analysis (TGA) was performed in a Thermogravimetric Analyzer Setaram Labsys EVO, both as external services from the Analysis Laboratory from LAQV-REQUIMTE, FCT-NOVA. Atomic Force Microscopy (AFM) images were acquired using an MFP-3D Stand Alone as an external service from CENIMAT facilities, from the i3N, NOVA School of Science and Technology.

Antibacterial assays were conducted in a STERIL-VBH laminar flux chamber. Bacterial suspension density was adjusted to the McFarland Scale with a DEN-1B McFarland Densitometer (Grant-Bio). Transparent, flat bottom 96 well plates were from Greiner Bio-One. Sterile swabs were from DeltaLab. 96-well plate and bacterial incubations were performed in a Mermmet Incubator B10. MICROTOX® Assays were conducted in a MICROTOX® M500 from ModernWater.

All compounds' chemical identities were verified using a combination of  $^1\text{H}$  NMR,  $^{13}\text{C}$  NMR,  $^{15}\text{N}$  NMR, 2D-COSY, 2D-HSQC, 2D-HMBC, and High-Resolution Mass Spectrometry. Using 5 mm tubes on a Bruker Avance II+ 600 spectrometer (Institute of Organic Chemistry with Centre of Phytochemistry-Bulgarian Academy of Sciences / NMR Centre), the  $^1\text{H}$  NMR and  $^{13}\text{C}$  NMR spectra were measured in DMSO-d<sub>6</sub> and CDCl<sub>3</sub> at 293.0 K at spectrometer operating frequencies of 600.13 MHz and 150.92 MHz, respectively. The  $^{15}\text{N}$  NMR spectra were obtained as  $^1\text{H}$ -/ $^{15}\text{N}$ -HSQC 2D spectra at 128 scans with a spectrometry frequency of 600.18 MHz / 60.83 MHz.  $^1\text{H}$  NMR and  $^{13}\text{C}$  NMR spectra were calibrated to the tetramethylsilane (TMS) signal,  $\delta = 0.00$  ppm. Chemical shifts were measured to an accuracy of 0.01 parts per million (ppm). The coupling constants ( $J$ ) were reported with a precision of 0.1 and represented in Hz. The spin multiplicity in the  $^1\text{H}$  NMR was denoted by the abbreviations s = singlet, d = doublet, t = triplet, q = quartet, dd = doublet of doublets, dt = doublet of triplets, td = triplet of doublets, and m = multiplet. Mestrelab Research S.L.'s MestreNova v. 15.0 was used to process the raw NMR data files.

High-Resolution Mass Spectrometry (HR-MS) analyses were performed in the Laboratory for Biological Mass Spectrometry–Isabel Moura (BIOSCOPE-PROTEOMASS Scientific Society Facility), using UHR ESI-Qq-TOF IMPACT HD (Bruker-Daltonics, Bremen, Germany). Samples of the corresponding compounds were prepared by dissolution in 50 % (v/v) acetonitrile containing 0.1 % (v/v) aqueous formic acid to obtain a working solution of 0.1  $\mu\text{g/mL}$ . HR-MS data was acquired by directly infusing the compound solutions into the ESI source. MS data were acquired in positive polarity over the mass range of 50 – 1300  $m/z$ . (Capillary voltage: 4500 V, End plate offset: -500 V, Charging voltage: 2000 V, Nebulizer gas: 0.4 Bar, Dry Heater: 180 °C, Dry gas: 4.0 L/min).

## 2.3. Computational details

We have employed the ORCA 6.0 software to perform density

functional theory (DFT) analysis and Avogadro to perform molecular visualization for the proposed metal complexes formed with compounds C1, C2 and C3 [35–40]. Firstly, a rough geometry adjustment was performed in the Avogadro software, through application of the Universal Force Field (UFF). Then, a Geometry Optimization function was performed using the ORCA 6.0 software, based on DFT calculations using the BP86 functional, based on the Becke exchange and Perdew correlation. The basis set used for these calculations was the def2-SVP. After the geometry optimization, the obtained coordinate file was visualized through the Avogadro and the UCSF Chimera softwares [41, 42].

## 2.4. Synthesis of naphthalimide-based derivatives

### 2.4.1. Synthesis of 2-allyl-6-bromo-1*H*-benzo[*d*]isoquinoline-1,3(2*H*)-dione (3)

4-Bromo-1,8-naphthalic anhydride (1) (3.100 g, 11.19 mmol, 1.0 eq) and allylamine (2) (0.703 g, 0.92 mL, 12.31 mmol, 1.1 eq.) were stirred in 25 mL dry DMF at 50 °C for 18 h. After cooling to room temperature, the reaction mixture was concentrated in vacuo. The formed precipitate was filtered and recrystallized from 30 mL (ethanol:water=25:5 v/v). The product was filtered and dried in vacuo to furnish 2.950 g (83 %) of compound 3 as an off-white powder.

$^1\text{H}$  NMR (600 MHz, d-DMSO)  $\delta$  8.51 (dd,  $J = 15.9, 7.8\text{ Hz}$ , 2 H), 8.28 (d,  $J = 7.8\text{ Hz}$ , 1 H), 8.18 (d,  $J = 7.8\text{ Hz}$ , 1 H), 7.96 (t,  $J = 7.9\text{ Hz}$ , 1 H), 5.93 (ddt,  $J = 15.7, 10.4, 5.2\text{ Hz}$ , 1 H), 5.19 – 5.10 (m, 2 H), 4.62 (d,  $J = 5.1\text{ Hz}$ , 2 H).  $^{13}\text{C}$  NMR (151 MHz, d-DMSO)  $\delta$  162.6, 162.6, 132.8, 132.6, 131.7, 131.4, 131.1, 129.8, 129.3, 128.9, 128.4, 122.7, 121.9, 116.5, 41.9, 39.9, 39.8, 39.7, 39.5, 39.4, 39.2, 39.1.

### 2.4.2. Synthesis of 2-allyl-6-((pyridin-2-ylmethyl)amino)-1*H*-benzo[*d*]isoquinoline-1,3(2*H*)-dione (C1)

Intermediate 3 (0.400 g, 1.27 mmol) and a large excess of 2-picolyamine (4) (2.00 mL) were mixed in 25 mL flask and heated at 95 °C for 18 h. After cooling to room temperature, the reaction mixture was dissolved in 80 mL DCM and washed with water. The organic phase was dried over anhydrous MgSO<sub>4</sub> and evaporated to dryness. TLC of crude product – DCM:MTBE = 5:1. The crude product was purified by column chromatography: 70 g silica gel; mobile phase DCM:MTBE = 7:1 v/v. The target product C1 was obtained in 0.425 g (98 %) as a yellow powder. M.p. 162–163 °C.

$^1\text{H}$  NMR (600 MHz, CDCl<sub>3</sub>)  $\delta$  8.68 (dd,  $J = 4.1, 0.8\text{ Hz}$ , 1 H), 8.60 (dd,  $J = 7.3, 1.0\text{ Hz}$ , 1 H), 8.49 (d,  $J = 8.3\text{ Hz}$ , 1 H), 8.34 (dd,  $J = 8.4, 0.8\text{ Hz}$ , 1 H), 7.75 (td,  $J = 7.7, 1.8\text{ Hz}$ , 1 H), 7.67 (dd,  $J = 8.3, 7.4\text{ Hz}$ , 1 H), 7.37 (d,  $J = 7.8\text{ Hz}$ , 1 H), 7.30 (dd,  $J = 6.6, 5.1\text{ Hz}$ , 1 H), 7.25 (s, 1 H), 6.73 (d,  $J = 8.4\text{ Hz}$ , 1 H), 6.00 (ddt,  $J = 17.1, 10.3, 5.7\text{ Hz}$ , 1 H), 5.33 – 5.26 (m, 2 H), 5.21 – 5.15 (m, 1 H), 4.79 (dt,  $J = 5.7, 1.3\text{ Hz}$ , 2 H), 4.67 (d,  $J = 4.2\text{ Hz}$ , 2 H).  $^{13}\text{C}$  NMR (151 MHz, CDCl<sub>3</sub>)  $\delta$  164.4, 163.9, 154.9, 149.1, 149.0, 137.0, 134.7, 132.7, 131.3, 129.9, 126.6, 124.8, 122.9, 122.8, 122.0, 120.6, 117.0, 110.3, 104.7, 77.2, 77.0, 76.8, 53.4, 47.3, 42.1, -0.02 (Figures SII-1 to SII-20).

Anal. calc. for C<sub>21</sub>H<sub>17</sub>N<sub>3</sub>O<sub>2</sub> (343.38): C, 73.45; H, 4.99; N, 12.24. Found: C, 73.40; H, 5.06; N, 12.29 %. ESI-MS: [M+H]<sup>+</sup> for C<sub>21</sub>H<sub>18</sub>N<sub>3</sub>O<sub>2</sub> = 344.1411 (5.1 ppm). Calculated [M+H]<sup>+</sup> for C<sub>21</sub>H<sub>18</sub>N<sub>3</sub>O<sub>2</sub> = 344.1393 (Figure SII4).

### 2.4.3. Synthesis of 2-allyl-6-((3-morpholinopropyl)amino)-1*H*-benzo[*d*]isoquinoline-1,3(2*H*)-dione (C2)

Intermediate 3 (0.300 g, 0.95 mmol) and a large excess of *N*-(3-Aminopropyl)morpholine 5 (3.00 mL) were mixed in a 25 mL flask and heated at 95 °C for 18 h. After cooling to room temperature, the reaction mixture was dissolved in 80 mL DCM and washed with water. The organic phase was dried over anhydrous  $\text{tK}_2\text{CO}_3$  and evaporated to dryness. TLC of crude product – MTBE:Et<sub>3</sub>N = 100:1. The final product was subjected to purification by column chromatography: 30 g silica gel; phase 1 MTBE:Et<sub>3</sub>N = 100:1; phase 2 MTBE:MeOH = 100:1 v/v.

Compound **C2** was obtained in 0.306 g (85 %) as a yellow powder. M.p. 174–175 °C.

<sup>1</sup>H NMR (600 MHz, CDCl<sub>3</sub>) δ 8.60–8.56 (m, 1 H), 8.45 (d, *J* = 8.4 Hz, 1 H), 8.27 (d, *J* = 8.1 Hz, 1 H), 7.73 (s, 1 H), 7.64–7.59 (m, 1 H), 6.63 (d, *J* = 8.5 Hz, 1 H), 6.00 (ddt, *J* = 15.9, 10.4, 5.7 Hz, 1 H), 5.29 (dd, *J* = 17.2, 1.4 Hz, 1 H), 5.20–5.15 (m, 1 H), 4.79 (d, *J* = 5.6 Hz, 2 H), 3.88 (t, *J* = 4.5 Hz, 4 H), 3.49 (q, *J* = 5.7 Hz, 2 H), 2.70–2.65 (m, 2 H), 2.61 (s, 4 H), 2.00 (s, 2 H). <sup>13</sup>C NMR (151 MHz, CDCl<sub>3</sub>) δ 164.5, 163.9, 150.5, 134.9, 132.7, 131.2, 129.9, 126.9, 124.2, 123.0, 120.4, 116.9, 109.4, 103.7, 77.2, 77.0, 76.8, 67.0, 59.2, 54.0, 44.7, 42.1, 23.1 (Figures SI2–1 to SI2–21). Anal. calc. for C<sub>22</sub>H<sub>25</sub>N<sub>3</sub>O<sub>3</sub> (379.45): C, 69.64; H, 6.64; N, 11.07. Found: C, 69.69; H, 6.60; N, 11.12 %. ESI-MS: [M+H]<sup>+</sup> for C<sub>22</sub>H<sub>26</sub>N<sub>3</sub>O<sub>3</sub> = 380.1969 (0.1 ppm). Calculated [M+H]<sup>+</sup> for C<sub>22</sub>H<sub>26</sub>N<sub>3</sub>O<sub>3</sub> = 380.1969 (Figure SI4).

#### 2.4.4. Synthesis of 2-allyl-6-((2-hydroxyethyl)thio)-1*H*-benzo[*de*]isoquinoline-1,3(2*H*)-dione (**C3**)

Intermediate **3** (0.400 g, 1.27 mmol), K<sub>2</sub>CO<sub>3</sub> (0.140 g, 1.01 mmol, 0.8 eq.) and a large excess of thiol **5** (5.00 mL) were mixed in a 25 mL flask and heated at 80 °C for 18 h. After cooling to room temperature, the reaction mixture was dissolved in 80 mL DCM and washed with water and citric acid. The organic phase was dried over anhydrous Na<sub>2</sub>SO<sub>4</sub> and evaporated to dryness. TLC of crude product – DCM: MTBE = 5:1. Analytical samples were obtained after purification by column chromatography: 70 g silica gel; mobile phase DCM:MTBE = 10:1 v/v. Compound **9** was obtained in 0.293 g (74 %) as a bright yellow powder. M.p. 129–130 °C.

<sup>1</sup>H NMR (600 MHz, d-DMSO) δ 8.49 (dd, *J* = 8.4, 1.0 Hz, 1 H), 8.47 (dd, *J* = 7.3, 1.0 Hz, 1 H), 8.30 (d, *J* = 7.9 Hz, 1 H), 7.84 (dd, *J* = 8.4, 7.3 Hz, 1 H), 7.73 (d, *J* = 8.0 Hz, 1 H), 5.92 (ddt, *J* = 17.1, 10.4, 5.3 Hz, 1 H), 5.17 (t, *J* = 5.5 Hz, 1 H), 5.15–5.09 (m, 2 H), 4.62 (d, *J* = 5.2 Hz, 2 H), 3.75 (q, *J* = 6.3 Hz, 2 H), 3.35 (t, *J* = 6.4 Hz, 2 H). <sup>13</sup>C NMR (151 MHz, d-DMSO) δ 162.6, 162.6, 144.5, 132.6, 130.8, 130.2, 129.6, 128.8, 127.4, 126.9, 123.3, 122.4, 118.3, 116.2, 59.1, 41.4, 39.9, 39.8, 39.7, 39.5, 39.4, 39.2, 39.1, 34.4 (Figures SI3–1 to SI3–17).

Anal. calc. for C<sub>17</sub>H<sub>15</sub>NO<sub>3</sub>S (313.37): C, 65.16; H, 4.82; N, 4.47; S, 10.23. Found: C, 65.19; H, 4.88; N, 4.41; S, 10.20 %. ESI-MS: [M+H]<sup>+</sup> for C<sub>17</sub>H<sub>16</sub>NO<sub>3</sub>S = 314.0848 (0.8 ppm) and [2 M+Na]<sup>+</sup> for C<sub>34</sub>H<sub>30</sub>N<sub>2</sub>O<sub>6</sub>S<sub>2</sub>Na = 649.1448 (1.6 ppm). Calculated [M+H]<sup>+</sup> for C<sub>17</sub>H<sub>16</sub>NO<sub>3</sub>S = 314.0845 and [2 M+Na]<sup>+</sup> for C<sub>34</sub>H<sub>30</sub>N<sub>2</sub>O<sub>6</sub>S<sub>2</sub>Na = 649.1437 (Figure SI4).

#### 2.5. Photophysical characterization and titrations

The naphthalimide derivatives **C1**, **C2** and **C3** were dissolved in dimethyl sulfoxide (DMSO), acetonitrile (ACN), absolute ethanol (EtOH), tetrahydrofuran (THF),  $\text{PCl}_3$  and toluene to a stock concentration of 10<sup>−2</sup> M. All studies were performed using the appropriate dilution of the stock solutions to a concentration of 10<sup>−5</sup> M. The UV-Vis absorption spectra measurements were collected in a JASCO V650 Spectrophotometer, and fluorescence spectra were acquired in a HORIBA Scientific FLUOROMAX-4 spectrofluorometer (BIOSCOPE-PROTEOMASS Scientific Society Facility). Solid-state spectra were also acquired with the HORIBA Scientific FLUOROMAX-4, using an optic fiber, through sample excitation at the appropriate wavelengths. Correction for the absorbed light was performed when needed. All measurements were performed at 25 °C.

For metal titrations, metal stock solutions were prepared in ACN, to a concentration of ca. 10<sup>−3</sup> M. Titrations were performed via the addition of the correct microliter quantities of each stock metal solution of the compounds at a concentration of 10<sup>−5</sup> M in THF, followed by the acquisition of the respective absorption and emission spectra.

Additional experiments were conducted to assess the selectivity of compounds **C2** and **C3** towards Hg<sup>2+</sup> metal ions. These experiments involved introducing an excess amount of other tested metal ions into a quartz cell containing the ligand and Hg<sup>2+</sup> metal ions. Subsequently,

absorption and fluorescence spectra were recorded to analyze any changes or interactions occurring in the presence of these competing metal ions.

Lifetime measurements were performed using a TEMPRO Fluorescence Lifetime System with a Nanoled pulsed diode controller from Horiba Jobin-Yvon (BIOSCOPE-PROTEOMASS Scientific Society Facility). Luminescence quantum yield was determined for compounds **C1** and **C2** using a solution of fluorescein in ethanol [ $\Phi$  = 0.79] [43], whereas, for compound **C3**, a coumarin 343 [ $\Phi$  = 0.63] [44] solution in ethanol was used.

The Logarithm of the Partition Coefficient [n-octanol/water] (logP) values were determined for all compounds following the liquid-liquid microextraction protocol, in which a saturated octanol solution of each compound was prepared to a concentration of ca. 1 g/L. 0.5 mL of this solution was added to 0.5 mL of MilliQ H<sub>2</sub>O, vigorously stirred, and allowed to rest for ca. 30 min. Then, the octanol phase was removed and quantified in a CLARIOStar spectrophotometer at 434, 445, and 396 nm for compounds **C1**, **C2**, and **C3**, respectively.

For the NMR experiments in the presence and absence of Hg<sup>2+</sup>, stock solutions (C = 0.01 M) of the free ligands (**C1**, **C2**, and **C3**) were prepared in DMSO-d<sub>6</sub>, which were divided into equal 600  $\mu$ L portions for the preparation of the working samples. A stock solution of mercury(II) acetate (C = 0.15 M) was also prepared in DMSO-d<sub>6</sub> and added into small aliquots to the free ligand solutions (0.0  $\mu$ L–0.00 eq., 5.0  $\mu$ L–0.12 eq., 10.0  $\mu$ L 0.25 eq., 20.0  $\mu$ L–0.50 eq., 40.0  $\mu$ L–1.00 eq., 80.0  $\mu$ L–2.00 eq., respectively) using automatic micropipettes. The final working solutions' concentrations determined to be C = 0.01 M. The operations for the sample preparations were carried out at ambient temperature.

#### 2.6. Naphthalimide-doped Polymers production

##### 2.6.1. PVC

200 mg of PVC were dispersed in 4 mL of THF and homogenized using ultrasonic treatment for ca. 2 min. Upon stabilization of the polymeric matrix, 0.5 mg of each compound was solubilized in 1 mL of THF, and the resulting solution was added dropwise to the stabilized polymeric matrix under gentle stirring. The mixture was stirred for ca. 2 min and plated onto a Teflon plate. The plate was allowed to dry in the dark at room temperature, under shaking at 40 rpm for ca. 24 h to ensure complete dryness and homogeneity of the polymer.

##### 2.6.2. PMMMA

300 mg of PMMMA were dispersed in 5 mL of chloroform under gentle stirring. 0.5 mg of each compound was solubilized in 1 mL of chloroform and the solution was added to the polymeric matrix suspension. The mixture was gently stirred for ca. 2 min and plated onto a Teflon plate and allowed to dry at room temperature, in the dark, under gentle shaking of 40 rpm for ca. 48 h to ensure complete dryness of the polymer.

##### 2.6.3. Starch

5 mL of warm Milli-Q H<sub>2</sub>O was added to 150 mg of Starch under vigorous stirring. The mixture was then heated and, after reaching 85 °C, was gently stirred for 5 min. 0.5 mg of each compound was dissolved in 1 mL of EtOH and added to the hot polymeric mixture. The mixture was gently stirred for another 5 min and was then plated onto a Teflon plate. The plate was stirred at 40 rpm, in the dark overnight to ensure the slow cooling of the polymer to room temperature. After ca. 24 h, the plates were placed in a hood at 40 °C and dried overnight to enable complete polymerization.

##### 2.6.4. Polymer characterization and heavy metal detection

First, all the obtained polymers were evaluated by naked-eye colorimetric assessment and under UV-Vis light. Solid-state spectra of all polymeric matrices were acquired to verify the entrapment of each compound inside the matrix. Moreover, FTIR-ATR spectra were

collected of all polymers in the spectral region of 400 to 4000 cm<sup>-1</sup>.

A range (0 to 10 µM) of aqueous Hg<sup>2+</sup> solutions was prepared, and the sensing response was evaluated in MilliQ H<sub>2</sub>O and Tap Water. For Starch polymers, squares of each polymer (ca. 0.5 × 0.5 cm) were cut and placed in contact with each solution for ca. 15 min. Before each incubation period, a visual evaluation was performed under UV light to verify the occurrence of any fluorometric alterations. Emission spectra for each solution were also recorded.

Limits of Detection (LOD) and Limits of Quantification (LOQ) were determined using ten measurements of a C2-Starch polymer lixiviate in water, without the addition of Hg<sup>2+</sup> metal ions. The following formulas were applied:

$$\text{LOD} = \text{ydl} = \text{yblank} + 3\text{std}, \text{ where ydl} = \text{signal detection limit and std} = \text{standard deviation.}$$

$$\text{LOQ} = \text{ydl} = \text{yblank} + 10\text{std}, \text{ where ydl} = \text{signal detection limit and std} = \text{standard deviation.}$$

From these formulas, the minimal detectable quantity (MDQ) and minimal quantifiable amount (MQA) were also determined.

## 2.7. Antibacterial activity assays

Selected bacterial strains for the assessment of inhibitory activity were *Escherichia coli* (E. coli, ATCC® 25922™), *Staphylococcus aureus* (ATCC® 6538™), methicillin-resistant *Staphylococcus aureus* (MRSA) (ATCC® 33591™), *Enterococcus faecalis* (ATCC® 29212™) and *Pseudomonas aeruginosa* (ATCC® 9027™). The bacteria were kept in adequate broth containing 15 % v/v glycerol at -70 °C. The stocks were thawed and inoculated onto TSA plates, followed by ca. 24 h of incubation at 35 ± 2 °C in a Mermmet Incubator B10. From the obtained bacterial colonies, bacterial suspensions were prepared with a density of 0.5 in the McFarland scale (DEN-1B McFarland Densitometer, Grant-bio) in a saline medium (0.85 % m/v), which translates to a bacterial concentration of ca. 1.5 × 10<sup>8</sup> CFU/mL.

### 2.7.1. Broth microdilution assays

Samples (compounds C1, C2, and C3) were dispersed in DMSO at a stock concentration of 1 mg/mL. A 2-fold dilution gradient was prepared in 96-well plates, in MHB to a maximum concentration of 0.76 µg/mL and a minimum concentration of 0.0015 µg/mL. Each well was inoculated with the prepared bacterial stocks to ensure a bacteria concentration of ca. 10<sup>-8</sup> CFU/mL for all tested bacterial strains. Then, the plates were incubated overnight at 35 ± 2 °C in a Mermmet Incubator B10. Bacteria and sample controls were also performed following the same protocol. After 24 h, the plates were collected, and the density measurements at 600 nm were performed using an adequate protocol in a CLARIOStar Spectrophotometer (BMG Labtech) (PROTEOMASS Scientific Society Facility). It was possible to determine the percentages of bacterial growth and Minimum Inhibitory Concentrations (MIC) in response to a specific condition by comparison with a positive bacterial control. All asepsis conditions were maintained throughout the assay by a STERIL-VBH laminar flux chamber.

### 2.7.2. Solid-state polymer assays

From the obtained bacterial stocks at 0.5 McFarland, a sterile swab was immersed in the solution and used to inoculate MHA plates. Polymers were cut into ca. 1 × 1 cm squares and applied on top of the inoculated plate. The plates were incubated at 35 ± 2 °C in a Mermmet Incubator B10 overnight. After 24 h, bacterial growth was visually evaluated in the contact interface polymer-agar.

## 2.8. Environmental Activity Assessment by Microtox® Test

To obtain a suitable solution for its application in the Microtox® Test, five 1 cm<sup>2</sup> squares of the C2 Starch doped polymer were submerged in 10 mL of Milli-Q H<sub>2</sub>O, until complete polymer solubilization was obtained. From the obtained solution, the Microtox® Whole Effluent

Toxicity (WET) Test was conducted as per the manufacturer's instructions. Briefly, a range of dilutions from 100 % to 6.25 % were prepared in the appropriate 2 % NaCl aqueous solution. The acute reagent comprised of freeze-dried *Vibrio fisheri*, was rehydrated with the appropriate Reconstruction Solution. Subsequently, 20 µL of the obtained bacterial suspension was then added to the diluted solutions and the luminescence of the bacteria was measured after incubation periods of 15 and 30 min. The obtained luminescence values for each sample were compared to the bioluminescence produced by the bacterial controls, and the % Effect was calculated accordingly for each condition.

## 3. Results and discussion

### 3.1. Synthesis of naphthalimide-based compounds

This work describes the design of three innovative probes derived from naphthalimide, aiming to create an efficient and affordable sensor platform using easily accessible chemicals.

Current sensors include a fluorophore – (naphthalimide core), and a receptor that enables them to function as a fluorescence switch. 1,8-Naphthalimide fluorophore was selected due to its superior photochemical properties, such as higher brightness and enhanced fluorescence quantum yield compared to other fluorophores [45]. This allowed for a more diverse platform for chemical transformations, resulting in significantly brighter and cheaper sensors. This strategic choice improved the sensitivity and specificity of metal ion detection, such as Hg<sup>2+</sup>. The receptor units, the 2-Picolylamine, N-(3-Aminopropyl)morpholine, and 2-Mercaptoethanol were chosen for their affordability and selectivity towards binding Hg<sup>2+</sup> metal ions.

Recently, Diamantis et al. reported the preparation of Zr<sup>4+</sup> metal-organic framework (MOF) based on a terephthalate ligand decorated with a chelating 2-picolylamine side group (dMOR-2 @CaA) for real-time detection of Cu<sup>2+</sup>, Pb<sup>2+</sup>, and Hg<sup>2+</sup> [46]. However, the authors reported that dMOR-2 @CaA effectively absorbed additional heavy metal ions, such as Cu<sup>2+</sup>, Cd<sup>2+</sup>, Ni<sup>2+</sup>, and Zn<sup>2+</sup>, when exploring the selectivity for dMOR-2 @CaA toward various heavy metal ions in aqueous media.

In an earlier study by Zhou et al., a dansyl derivative with an aminomorpholine moiety selectively coordinated mercury ions [47]. Nevertheless, their studies were conducted in MeCN: H<sub>2</sub>O (4:1 v/v) media, while a complete "turn-off" effect was achieved at Hg<sup>2+</sup> concentrations reaching 150 µM.

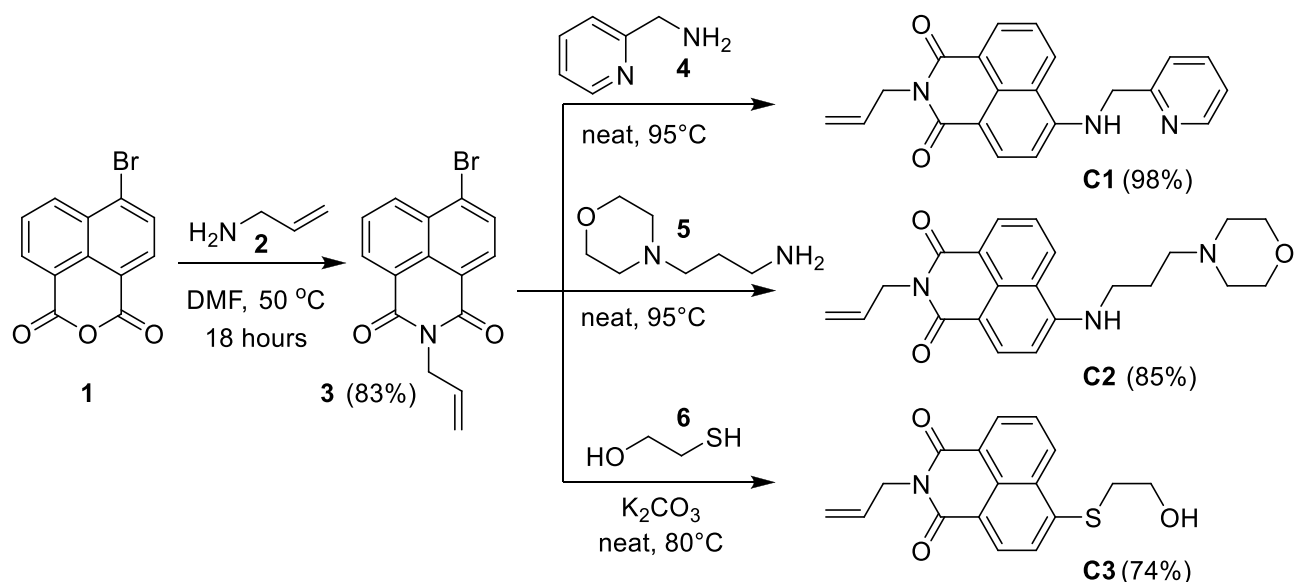
Recent studies by Gao et al. revealed that a mercaptoethanol fragment not only increased the water solubility of the proposed sensors but was a suitable receptor for Hg<sup>2+</sup> ions due to the presence of sulfur [48]. Despite the proven sensing capabilities of the reported molecules, according to the authors, their response to Hg<sup>2+</sup> was almost completed within 30 min, which was a somewhat lengthy incubation period.

Considering all these factors, our approach focuses on creating uncomplicated, biodegradable, eco-friendly, and cost-effective probes for the rapid detection of hazardous ions.

Three naphthalimide derivatives were synthesized in this work and are depicted in Scheme 1. The first synthetic step included the preparation of key intermediate product 3 by the implementation of a literature procedure, where bromonaphthalic anhydride (1) and allylamine (2) were boiled in ethanol [49–51], which is a typical approach. In the current synthetic protocol, we employed DMF as the solvent, and 50 °C was used as the reaction temperature.

Target compounds C1 and C2 were obtained in good to excellent yields by heating 3 with an excess of amines 4 and 5, respectively. Heating of 3 with an excess of thiol 6 in the presence of K<sub>2</sub>CO<sub>3</sub> led to the preparation of target compound C3.

Some analogs of C1 - C3 bearing different substituents at the imide nitrogen were studied as fluorescent detectors. Thus, some analogs of C1 served as detectors of palladium and cell imaging [52], while others were appropriate for monitoring protein-DNA interactions [53]. Hanaoka et al. presented off-on fluorescent chemosensors for Zn<sup>2+</sup> ions



**Scheme 1.** Synthetic approach to the preparation of the target naphthalimide fluorophores.

[54], while Wang *et al.* used a similar compound for the detection of Cu<sup>2+</sup> ions. Naphthalimide derivatives of 3-morpholinopropan-1-amine were suitable for lysosome markers [55]. Thioalcohols (similar to C3) were used as glutathione fluorescent indicators [56].

Analytical samples of all compounds were obtained after column chromatography and fully characterized by 1D and <sup>2</sup>D NMR analysis, HRMS, and melting points.

### 3.2. Spectroscopic characterization of compounds

The optical properties of compounds C1 and C2 were evaluated in the following solvents: DMSO, ACN, EtOH, THF, chloroform and toluene, at 25 °C. Compound C3 was also tested in the aforementioned solvents, except for toluene. A complete spectroscopic characterization of all compounds was performed and is summarized in Fig. 1 and Table 1. Compounds C1 and C2 exhibited an intense yellow naked-eye coloration in all solvents and strong yellow-green fluorescence under a

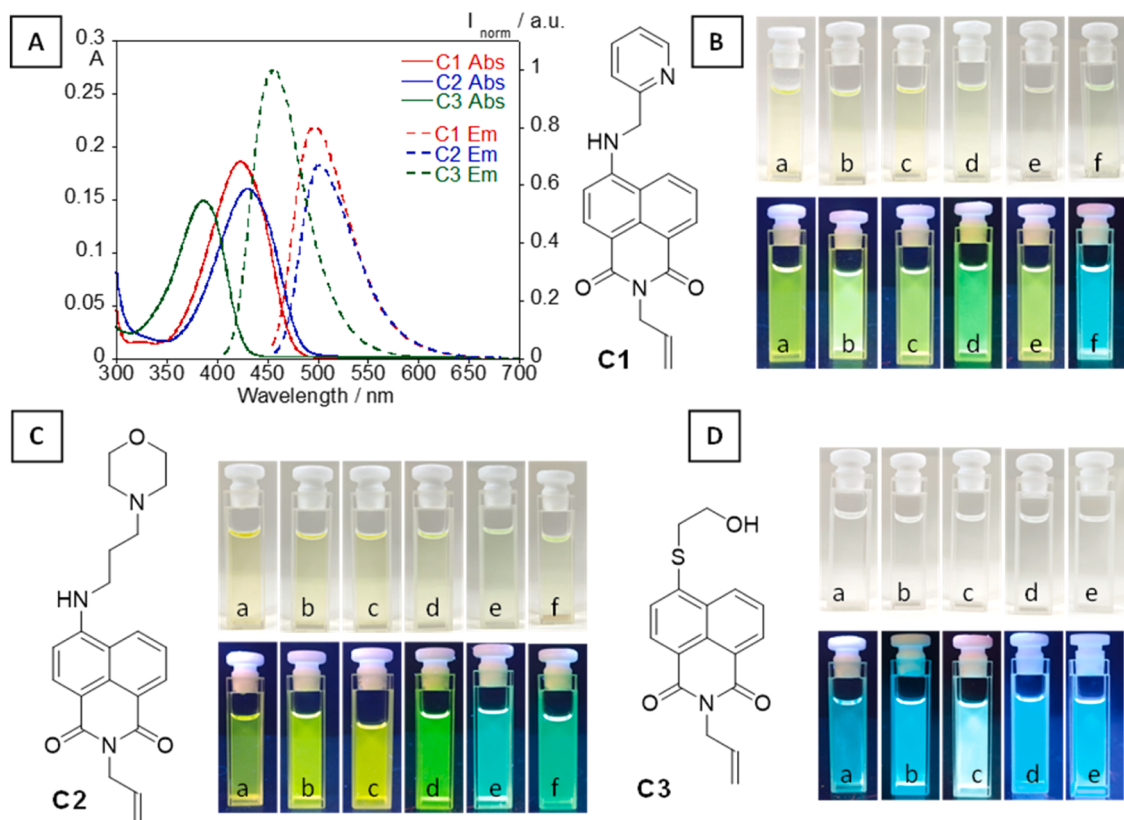


**Fig. 1.** (A) Absorption and emission spectra of C1, C2, and C3 in THF. ([C1-C3] = 10<sup>-5</sup> M, λ<sub>excC1</sub> = 423 nm, λ<sub>excC2</sub> = 430 nm, λ<sub>excC3</sub> = 387 nm, T = 25°C). C1 (B), C2 (C), and C3 (D) solutions (top: naked eye; down: under a UV lamp) in all tested solvents: a) DMSO; b) ACN; c) EtOH; d) THF; e) Chloroform; f) Toluene.

**Table 1**

Main photophysical data of the naphthalimide derivatives C1, C2 and C3.

Cpd.	Solvent	$\lambda_{\text{abs}}$ (nm)	$\lambda_{\text{em}}$ (nm)	$\lambda_{\text{em}}^{\text{solid}}$ (nm)	Stokes Shift (cm $^{-1}$ )	$\epsilon$ (cm $^{-1}$ M $^{-1}$ )	$\Phi$ (%)	$\tau$ (ns)
C1	DMSO	438	523	533	3700	16174	60	10.16 ± 0.01
	ACN	425	511		3900	19663	39	10.02 ± 0.01
	EtOH	432	521		3900	16554	49	9.06 ± 0.01
	THF	423	496		3500	18917	40	9.09 ± 0.01
	CHCl <sub>3</sub>	409	493		4200	18416	40	9.33 ± 0.01
	Toluene	419	481		3000	18936	46	7.68 ± 0.01
C2	DMSO	445	526	534	3500	18284	93	8.35 ± 0.09
	ACN	435	522		3800	17922	69	7.14 ± 0.01
	EtOH	442	527		3600	20898	93	5.60 ± 0.01
	THF	430	501		3300	16307	87	9.46 ± 0.01
	CHCl <sub>3</sub>	425	488		3000	17719	39	9.13 ± 0.01
	Toluene	427	486		2800	22369	52	8.33 ± 0.01
C3	DMSO	394	484	502	4700	14691	11	8.17 ± 0.02
	ACN	386	468		4500	15264	59	7.47 ± 0.01
	EtOH	390	478		4700	14443	74	6.77 ± 0.01
	THF	387	458		4000	13552	64	6.65 ± 0.01
	CHCl <sub>3</sub>	386	450		3700	13086	69	6.33 ± 0.01

UV-Vis lamp. In contrast, compound C3 did not show visible naked-eye coloration in any solvent, although it exhibited a strong blue fluorescence. Solid state spectra of all compounds are depicted in the Supplementary Material (Figure S15).

As a representative case, Fig. 1A shows the absorption and emission spectra of compounds C1, C2, and C3. The absorption bands centered at 423, 430, and 387 nm for C1, C2, and C3 were characteristic of general  $\pi - \pi^*$ -transitions of the naphthalimide chromophore. The increased number of donor atoms and aromatic rings attached to the naphthalimide scaffold produced a red shift in the absorption spectra. The same observation was verified in the excited state, where C1, C2 and C3 exhibited maximum emission bands at 496, 501, and 458 nm, respectively.

A significant blue shift was observed for compound C3, derived from the presence of a sulfur atom in its structure, providing the compound with a strong blue fluorescence. Sulfur, a larger atom with a different electron distribution and lower electronegativity than oxygen or nitrogen, can affect the molecule's electronic structure. Moreover, the presence of electron-withdrawing groups typically resulted in a blue shift.

Naphthalimides can exhibit pronounced solvatochromic behavior due to their  $\pi$ -electron system and the presence of functional groups (imide group) that can interact with the solvent [57–59]. In turn, a significant solvatochromic effect was observed in the excited state, visually detected by the coloration change under a UV lamp (Fig. 1B, C, and D). The solvatochromic shifts were most pronounced for compounds C1 and C2 with increasing solvent polarity. Specifically, for C1, the color transition occurred from blue (toluene) to yellow-green, while for C2, the color shifted from green to yellow. These changes demonstrated a positive solvatochromic behavior.<sup>r</sup>

To better understand the occurring solvent-compound interactions, a multiparametric fit analysis was performed by the application of the Kamlet-Taft equation [60] (Equation 1).

$$\nu = \nu_0 + a\alpha + b\beta + p\pi^*$$

#### Equation 1. Kamlet-Taft Equation.

This mathematical model enabled the determination of parameters related to solute-solvent interactions that ultimately depended on specific solvent parameters and provided a greater understanding of several physicochemical properties, such as the effects of different solvents on the stability of molecules and solvatochromic behavior. Particularly, this model employed the specific hydrogen bond donating (HBD) acidity ( $\alpha$ ), hydrogen bond accepting (HBA) basicity ( $\beta$ ), and solvent dipolarity/polarizability ( $\pi^*$ ) of each solvent. Tables 2 and 3 represents some relevant solvent spectroscopic properties for the application of the model.

**Table 2**

Spectroscopic polarity parameters and physical properties of the different solvents.  $\epsilon_r$ : relative permittivity;  $\eta$ : refractive index;  $\alpha$ : the solvent HBD acidity;  $\beta$ : solvent HBA basicity;  $\pi^*$ : solvent dipolarity/polarizability.

Solvent	$\epsilon_r$	$\alpha$	$\beta$	$\pi^*$	$\eta$
DMSO	47.24	0	0.76	1.00	1.47
ACN	35.94	0.19	0.40	0.66	1.34
EtOH	24.30	0.86	0.75	0.54	1.36
THF	7.58	0	0.55	0.58	1.40
CHCl <sub>3</sub>	4.89	0.20	0.10	0.69	1.44
Toluene	2.38	0	0.11	0.49	1.49

**Table 3**

Kamlet-Taft multiparametric fitting of emission data for each compound:  $\nu_0$ , a, b and p-values, in cm $^{-1}$ , slope and correlation coefficients ( $R^2$ ).

	$\nu_0$	a	b	p	Slope	$R^2$
C1	21840	-921	-1140	-1844	1.00	0.99
C2	21382	-628	-1749	-988	1.00	0.98
C3	23890	-762	-1679	-1952	1.00	1.00

The fitted parameters (a, b, and p), as well as the respective slopes and correlation coefficients, were obtained through the fitting of a linear plot of  $\nu_{\text{exp}}$  versus  $\nu_{\text{calc}}$ , obtained by application of the Kamlet-Taft model.  $\nu_0$  is representative of the value of emission in a reference solvent.

Parameters a (hydrogen bond acceptor sensitivity), b (hydrogen bond donor sensitivity), and p (dipolarity/polarizability sensitivity) were used to describe the solvatochromic behavior of compounds, specifically how their electronic properties, such as absorption or emission spectra, changed with the solvent environment.

Interestingly, all compounds exhibited negative values for both a and b, with the magnitude of b being greater than a. This observation indicated that naphthalimide derivatives were strong hydrogen bond acceptors. For example, their electronic characteristics were influenced by solvents with high hydrogen bond donating abilities.

Moreover, the results revealed that compound C3 was more influenced by solvent dipolarity/polarizability than compounds C1 and C2. A significant negative  $\pi^*$ -value for compound C3 suggested that it became less stable in highly polar or polarizable solvents. On the contrary, compound C2 was more stable in polar solvents than compounds C1 and C3.

Additionally, as naphthalimide-based compounds tended to present bioactive characteristics, the logarithm of the Partition Coefficient [ $n$ -

Octanol/Water] ( $\log P$ ) was determined through UV-Vis based methodology for compounds C1–C3.  $\log P$  is an indicator of the hydrophilicity of a determined compound, which can act as a characterizing metric for the propensity of a compound to migrate from an aqueous phase to a lipophilic one. The higher the  $\log P$  value, the more hydrophobic the compound, whereas a low  $\log P$  value indicates a more lipophilic compound. These variations can also be interpreted from a biological perspective, where a higher  $\log P$  value relates to the ability of a compound to transverse a lipophilic environment, such as cell membranes. The calculated values of  $\log P$  were 3.32, 1.52 and 2.46 for compounds C1, C2, and C3, respectively. These results were in accordance with those obtained through a theoretical calculation performed using the ChemDraw software, in which the obtained results were 2.99, 1.88, and 2.60, respectively. Furthermore, the obtained results for compound C1 show that it possesses a higher lipophilicity, thus being more likely to transverse cellular membranes.

### 3.3. Polymer production

To produce a solid support matrix for compounds C1, C2, and C3, they were incorporated into three polymeric matrices: PVC, PMMMA, and Starch. Incorporation of the compounds on PVC and PMMMA matrices employed a protocol previously developed by our group [61]

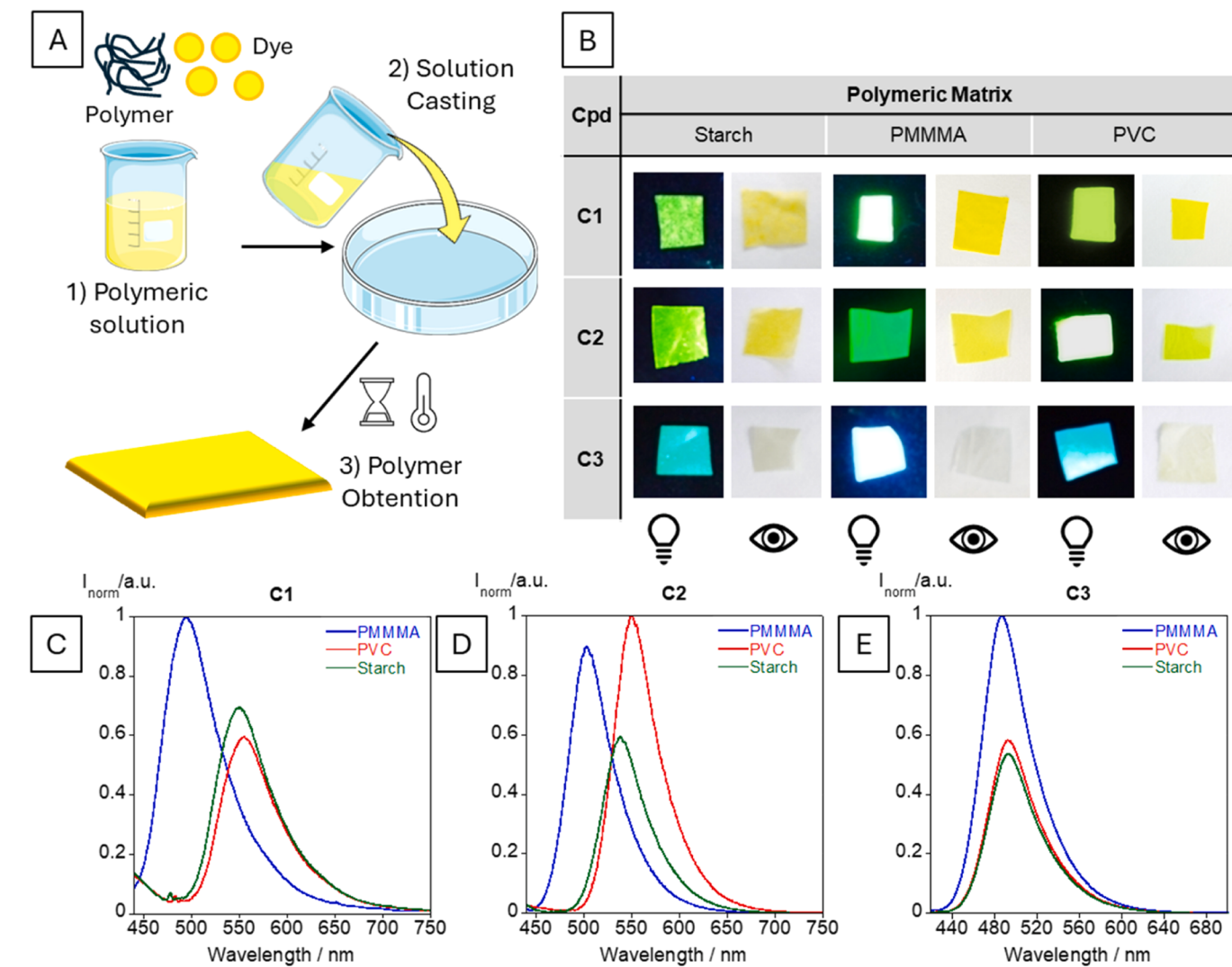


**Fig. 2.** (A) Schematic overview of the solvent-casting methodology employed for polymer production in this work. (B) Polymers obtained with compounds C1, C2 and C3. For all polymers, a constant mass of 0.5 mg was maintained for each compound. Solid-State emission spectra of C1 (C), C2 (D) and C3 (E) doped polymers.

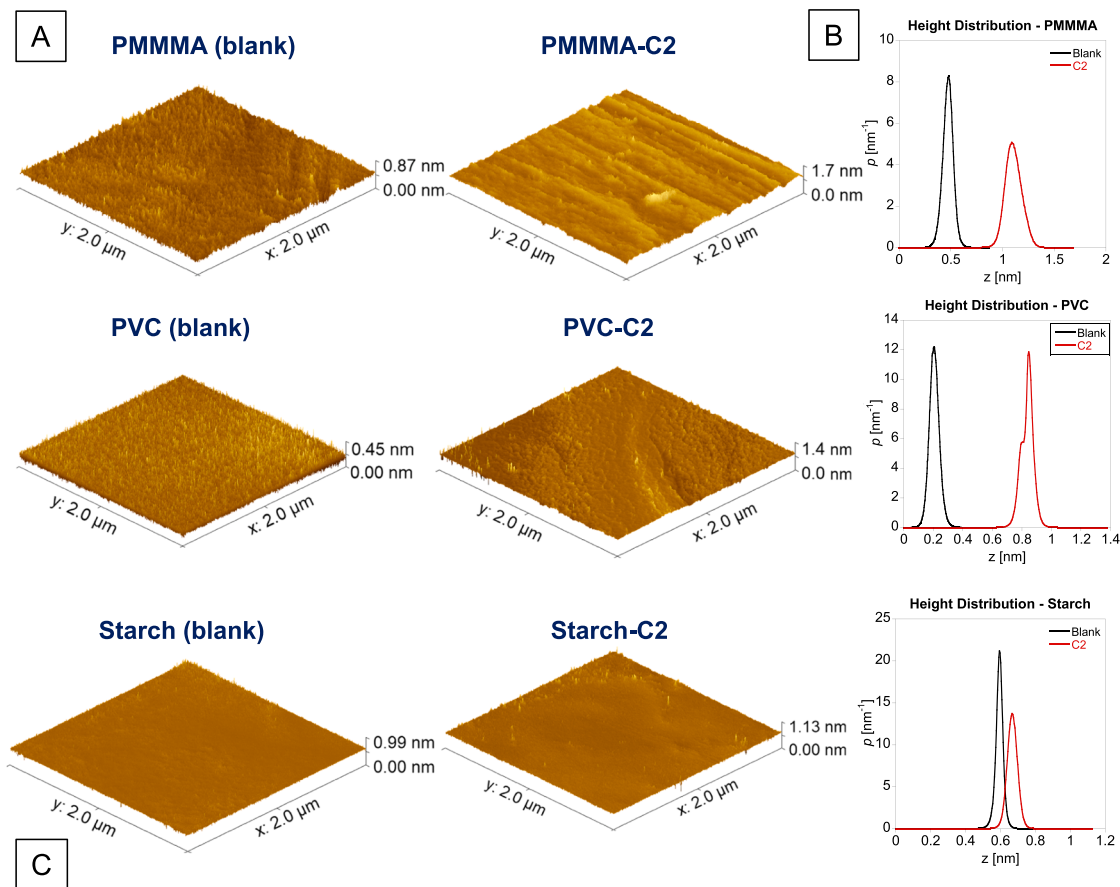
and was based on a simple solvent-casting methodology.

Therefore, each compound was incorporated into each polymeric matrix by dissolving it in the appropriate solvent: THF for PVC, ethanol for Starch, and chloroform for PMMMA. The appropriate amounts of polymer were also dispersed in the respective solvents and briefly stirred to form a soluble, fully dispersed, and homogeneous polymeric matrix. Upon stabilization of the polymeric matrix, the solubilized compound was added, under stirring, to ensure the entrapment of the compounds in the matrices and their complete dispersion once dried. An important aspect to consider when performing compound entrapment in polymeric matrices is the compatibility of solvents between compounds and the matrices themselves. The usage of the same or compatible solvents facilitates the complete dispersion of the compounds in the matrix, without the formation of inner precipitates. The applied methods herein produced dispersed, homogeneous polymers with a high emissive intensity, mimicking the effects observed in solution (Fig. 2A and B).

In the case of the Starch matrix, a simple solvent casting methodology at room temperature was insufficient to ensure polymerization. For example, to achieve stabilization of the polymeric matrix in solution and allow the compound to be incorporated, the mixture needed to be stabilized at 85 °C. Several studies in the literature showed the different effects that temperature may have on the polymerization of Starch, mainly dependent on annealing processes [62]. Briefly, annealing is

commonly used in metallurgy and material science to define a process by which a matrix is heated and cooled under controlled circumstances to modify its physical characteristics. These temperature cycles permit structural modifications such as the crystallization of the amylose and

amylopectin monomers in Starch. A well-defined, tri-dimensional Starch mesh is produced, allowing for the incorporation of compounds in the matrix. In this study, several temperatures were tested, ultimately showing that the optimal conditions for producing a well-dispersed



Sample	Thermal decomposition temperature (°C)	%Weight loss (%)	Glass Temperature (°C)	RMS roughness (pm)	Medium height (Z) (nm)
PMMMA	124.8	14	105	52.13	0.48
PMMMA C2	130.2	13	119-122	83.15	1.09
PVC	118.2	11	85	35.17	0.21
	279.6	40			
PVC C1	115.6	9	85		
	258.2	46			
PVC C2	124.3	10	86	43.40	0.85
	261.7	49			
Starch	86.6	9	-	31.51	0.60
	293.8	39			
Starch C1	100.0	5	-		
	295.8	35			
Starch C2	108.7	7	-	76.78	0.67
	295.6	38			

**Fig. 3.** (A) Atomic Force Microscopy (AFM) (3-D topographical) images, corresponding height distribution profiles (B) and (C) DSC, TGA, and AFM main characterization data of the neat polymers (PMMMA – blank, PVC – blank, Starch – blank) and respective C2 - doped polymer films.

polymer were at 85 °C under vigorous stirring. The compounds were then added to the Starch solution, allowing for a homogeneous dispersion in the pre-polymerized matrix. After this incorporation step, the cooling step was crucial for the crystallization and polymerization of the matrix. To ensure the complete dispersibility of the compounds in the polymer, we allowed them to cool to room temperature under a gentle stirring of ca. 40 rpm. Upon reaching room temperature, the compound, and the amylose and amylopectin monomers achieved stabilization, and the second temperature cycle was applied at 40 °C to dry the polymer. This two-step temperature-dependent cycle was found to produce homogeneous, well-dispersed water-soluble polymers without the use of plasticizer molecules and harsh chemicals.

Intriguingly, upon incorporation in a polymeric matrix, the compounds exhibited a blue shift in emission in response to polymer rigidity, demonstrating a tendency already reported by our group [61]. A more rigid polymeric matrix resulted in stronger intermolecular interactions between the doped compounds and the respective polymeric matrix. The PMMMA polymer was a more rigid material than the PVC and Starch polymers, so the compounds demonstrated a stronger blue shift in the emission bands. The maximum emission wavelengths for compound C1 were 495 nm, 550 nm, and 555 nm; for compound C2, were 503 nm, 538 nm, and 550 nm; and for compound C3 were 487 nm, 493 nm, and 494 nm, respectively, for PMMMA, Starch and PVC polymers (Fig. 2C, 2D and 2E). The less rigid matrices with Starch and PVC generated more varied interactions between the compounds and the matrices, resulting in red-shifted bands. Additionally, the polymers were characterized by Infrared (FTIR-ATR) spectra (Figures S16–8).

The FTIR-ATR spectra of PMMMA, PVC, and Starch, as well as C1, C2, and C3 dye-doped polymers, revealed significant interactions between the polymers and the dyes. For PMMMA, characteristic peaks at 2950 cm<sup>-1</sup> (C-H stretching), 1720 cm<sup>-1</sup> (C=O stretching), and 1140 cm<sup>-1</sup> (C-O-C stretching) showed slight shifts and intensity changes upon dye doping, indicating interactions with the dyes.

For PVC, the peaks located at 2950 cm<sup>-1</sup> (C-H stretching), 1420 cm<sup>-1</sup> (CH<sub>2</sub> bending), and 700 cm<sup>-1</sup> (C-Cl stretching) were shifted, especially in PVC-C1, suggesting strong dye interaction. The spectra for Starch exhibit characteristic peaks at 3300 cm<sup>-1</sup> (O-H stretching), 2920 cm<sup>-1</sup> (C-H stretching), and 1000–1200 cm<sup>-1</sup> (C-O stretching). These peaks were modified by dye doping, indicating changes in the hydrogen bonding and glycosidic bonds [63].

Due to the low concentration of dyes in the doped polymers compared with the polymer matrix, it was not possible to identify the specific dye peaks in the spectra. The observed changes primarily reflected the influence of the dyes on the polymer matrices rather than the distinct spectral features of the dyes themselves. Overall, the spectral changes highlighted how each dye uniquely affected the polymer matrices, suggesting varying degrees of chemical and physical interactions.

To ensure and validate the proper integration of the compound into the polymer matrix, the most promising polymers were selected for differential scanning calorimetry (DSC), thermogravimetric (TGA), and atomic force microscopy (AFM) analyses.

DSC and TGA were performed to investigate changes in the physical properties of PMMMA, PVC and Starch doped with compounds C1 and C2 in a temperature range from 29 °C to 300 °C. Fig. 3 and S19–11 show the obtained spectra and main characterization data, for the tested doped polymers.

The TGA spectra for PMMMA and PMMMA-C2 exhibited a typical thermal degradation behaviour with endothermic transitions. Both samples showed a similar percentage of mass loss (14 % and 13 %), indicating the release of volatile products due to polymer decomposition. The C2-doped PMMMA polymer exhibited higher decomposition temperatures (130.2 °C), suggesting greater thermal stability compared to the blank (124.8 °C). The glass transition temperature ( $T_g$ ) for the PMMMA-C2 polymer was 119–122 °C, a significantly higher value than the typical  $T_g$  (105 °C) [61] for PMMMA. The observed elevated  $T_g$

indicated enhanced thermal stability and confirmed the successful entrapment of the dye within the polymeric matrix. The dye incorporation increased chain entanglement and reduced the mobility of the polymeric chains, contributing to improved thermal properties.

All three PVC samples had  $T_g$  values of ca. 85 °C, with minor variations. C2-doped PVC had the highest  $T_g$  (86 °C), followed by the other PVC polymers. Additionally, this sample presented higher thermal stability owing to its higher decomposition temperatures and more significant mass loss in the second transition (49 % for C2, 46 % for C1). The observed mass loss was due to the de-hydrochlorination of the polymer chain, accompanied by endothermic events [64] confirming the successful entrapment of the dye into the polymeric matrix [65].

The results obtained for the Starch-based polymers also provided insights into their thermal behaviour. Although the samples showed similar decomposition patterns, C2-doped Starch polymer exhibited enhanced thermal stability in the first decomposition phase. Overall, the successful doping of PMMMA, PVC, and Starch with C1 and C2 dyes was evidenced by the doped polymers increased thermal stability and higher  $T_g$  values. The enhanced properties were attributed to the effective entrapment of the dyes within the polymeric matrices. These thermal analysis results were aligned with the obtained AFM images.

The AFM images in Fig. 3 show the topographical differences between the free and C2-doped polymers. The PMMMA polymers showed a roughness of 0.87 nm, which increased to 1.7 nm after C2 incorporation. A similar result was found for the other doped polymers, with surface roughness increasing from 0.43 nm to 1.4 nm and 0.39 nm to 1.18 nm for the PVC blank, Starch blank, and C2 post-incorporation polymers, respectively. Additionally, in all cases a shift was observed in the height distribution towards greater roughness in C2-doped polymer compared to the blank, suggesting the successful incorporation of compound C2 [66].

Based on the AFM results, C2-doped Starch was the best choice for future applications owing to the relatively uniform increase in surface roughness and more homogeneous texture, while being environmentally friendly.

### 3.4. Metal sensing ability of naphthalimide<sup>+</sup> derivatives in solution and within polymer-supported structures

The metal sensing ability of compounds C1, C2 and C3 was initially evaluated against Ag<sup>+</sup>, Cd<sup>2+</sup>, Ni<sup>2+</sup>, Co<sup>2+</sup>, Cu<sup>2+</sup>, Zn<sup>2+</sup>, Cr<sup>3+</sup>, Fe<sup>2+</sup>, Fe<sup>3+</sup>, Al<sup>3+</sup> and Hg<sup>2+</sup> metal ions. Both absorption and emission spectra were acquired at 25 °C until a plateau was reached. Compound C1 sensed both Hg<sup>2+</sup> and Cu<sup>2+</sup> ions, while compounds C2 and C3 were only highly selective towards Hg<sup>2+</sup> metal ions. Fig. 4, S12, and S13 show the absorption and emission spectra for the titrations that present a significant spectral change.

Compound C1 was found to interact with two metal ions, namely Cu<sup>2+</sup> and Hg<sup>2+</sup>, as depicted in Fig. 4. When the concentration of Cu<sup>2+</sup> increased, the absorbance at 423 nm decreased, along with a quenching in the emission intensity at 496 nm. This behavior was presumably attributed to the unique paramagnetic properties of Cu<sup>2+</sup> metal ions, derived from its unfilled *d* orbital shells. Such characteristics make Cu<sup>2+</sup> ions particularly sensitive to the chelation enhancement of quenching (CHEQ) effect, which is mostly driven by electron or energy transfer [67].

A similar quenching effect in fluorescence spectra was found by adding Hg<sup>2+</sup> metal ions to the ligand. This effect may be derived from the heavy atom nature of Hg<sup>2+</sup>, which exhibits a high electron count in its outer shells and can interact with the excited-state electrons of a fluorophore through spin-orbit coupling, since they are naphthalimide-based molecules [68]. These interactions potentiate the occurrence of non-radiative decay pathways, which lead to the deactivation of the excited state and thus, a visible quenching effect. In the ground state, no significant alterations were visualized with the increasing amount of added Hg<sup>2+</sup> ions.

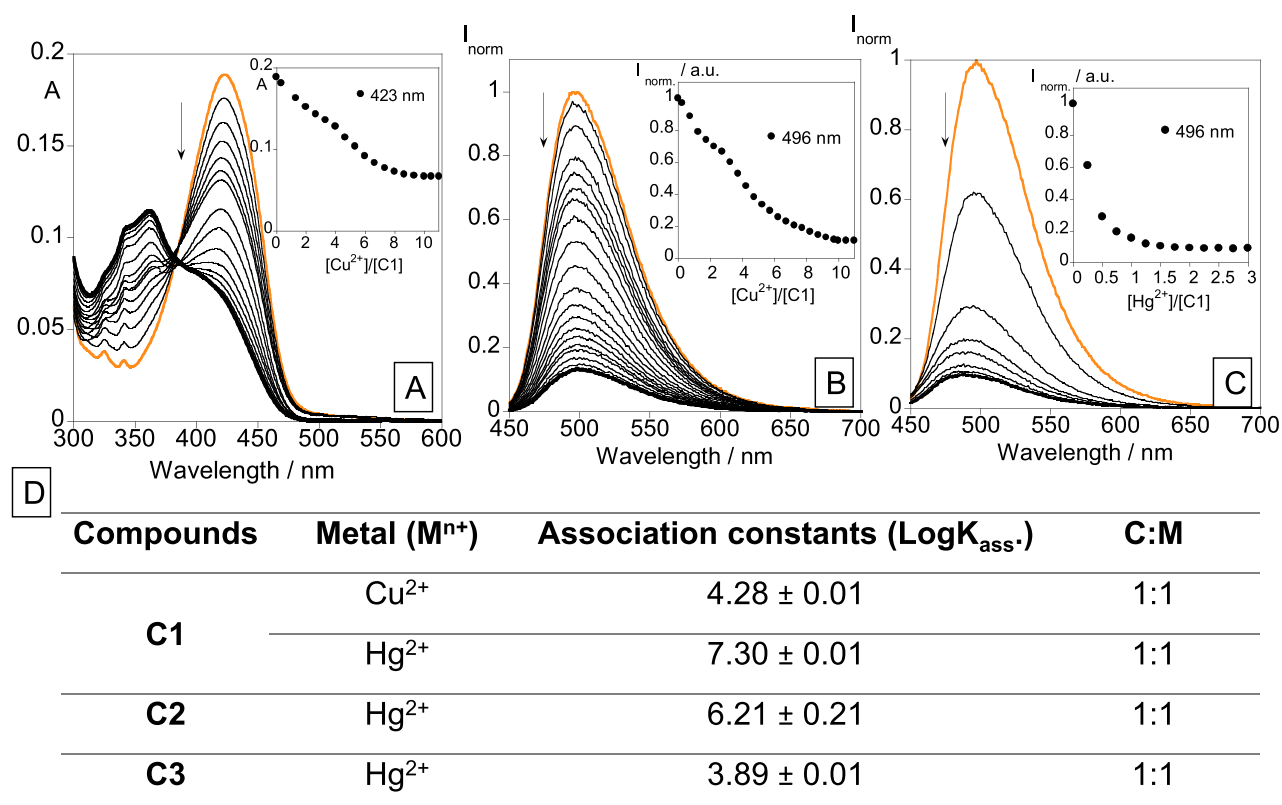


**Fig. 4.** (A, B, C) Spectrophotometric and spectrofluorimetric titrations of compound C1 with increased additions of  $Cu^{2+}$  (A, B) and  $Hg^{2+}$  (C) metal ions in THF. Insets depict absorption (A) and emission (B, C) as a function of equivalents of  $Cu^{2+}$  and  $Hg^{2+}$ , respectively.  $[C1] = 10^{-5} M$ ,  $\lambda_{exc} = 423 nm$ ,  $T = 25^\circ C$ . (D) Stability association constants and stoichiometry (C:M) of C1, C2 and C3 complexation with  $Cu^{2+}$  and  $Hg^{2+}$  metal ions, in THF.

Compounds C2 and C3 only showed significant spectral changes in response to  $Hg^{2+}$  metal ions (Figures SI12 and SI13). In the case of compound C2, a red shift from 430 nm to 465 nm and an increase at 465 nm was observed in the absorption spectra. Conversely, a blue shift from 505 nm to 485 nm was found in the emission spectra. Moreover, before the shift occurred in the emission spectra, a quenching mechanism took place, decreasing the emission intensity of the compound.

For compound C3, no significant alterations were found in the absorption spectra, although a significant quenching effect occurred in the emission spectra. Once again, this fluorescence attenuation may be due to the heavy atom effect, as explained above for compound C1.

Compounds C2 and C3 demonstrated a sensory selectivity for  $Hg^{2+}$  metal ions, hence, competition studies were performed to better understand these interactions. A constant excess of each remaining metal ion was added to the compound- $Hg^{2+}$  complexes, and their absorption and emission spectra were recorded. The spectral results are presented in the *Supplementary Material* (Figures SI14 and, SI15). No significant spectral alterations were observed when the remaining metal ions were added to the compound- $Hg^{2+}$  complex. Therefore, these compounds were selective for  $Hg^{2+}$  metal ions even in the presence of other metal species in solution.

To further comprehend the metal-ligand interactions, the stability constants, respective to each significant titration, were calculated using the HypSpec program [69,70], and the obtained values are summarized in Fig. 4D.

Analyzing the obtained results revealed a strong affinity of compounds C1 and C2 to  $Hg^{2+}$  metal ions. Compound C1, while capable of binding to  $Cu^{2+}$  metal ions, showed a clear preference for interacting with  $Hg^{2+}$ , as evidenced by the highest association constant ( $LogK_{ass.} = 7.30 \pm 0.01$ ), with a stoichiometry of one ligand per metal ion. A near value was also obtained for compound C2 with  $Hg^{2+}$ , with an association constant of  $LogK_{ass.} = 6.21 \pm 0.21$ , accompanied by  $Hg^{2+}$

selectivity. The investigated complexes' stability constants showed the formation of mononuclear species for all obtained complexes. Mass spectrometry of the  $Cu^{2+}$  and  $Hg^{2+}$ -formed complexes was performed as a validation method. The obtained spectra are shown in Figure SI16. For compound C1, the  $Cu^{2+}$  and  $Hg^{2+}$  mononuclear species were successfully identified at 344.1394  $m/z$  and 546.1103  $m/z$ . The  $Hg^{2+}$ -C2 complex was observed in the mass spectra at 380.1969  $m/z$  (Figure SI16). In the case of C3, no metal complexes were observed, possibly due to the lower association constant.

$Hg^{2+}$  ions typically coordinate with ligands with soft donor atoms, and while sulfur is a common donor, nitrogen atoms, particularly those in aromatic rings such as pyridines or imidazole, are also effective in binding mercury. In a complex, the special arrangement, length, and flexibility of the spacer, as well as the nature of the donor atoms of the compounds, are crucial. So, to best understand the coordination mechanisms in place for the herein studied complexes, additional NMR titration studies and theoretical calculations were performed for the obtained complexes (Fig. 5 and SI17–20). Considering compound C1, upon the addition of an excess of  $Hg^{2+}$  metal ions, a broadening of the  $^1H$  NMR signals was verified, being the first indicator of the complexation, as seen in Fig. 5D. Additionally, minor changes of the chemical shifts were also observed for all CH signals of the pyridine ring (ca. 7.30–8.60 ppm), and to a less extent, some of the peaks correspondent to the naphthalimide core also suffered alterations (ca. 8.80–6.65 ppm). A stronger alteration could, however, be verified for the  $CH_2$  group at ca. 4.74 ppm, linking the NH group to the pyridine heterocycle, being indicative of the role that both nitrogen atoms present in the structure have towards the complexation mechanism. Additionally, no significant spectral alterations were observed in the allyl fragment of the molecule, suggesting that these do not contribute to the complexation mechanisms. Significant alterations on both nitrogen atoms were also observed in the  $^{15}N$  NMR spectra, as seen in Fig. 5E, with a shift of 44.22 ppm to

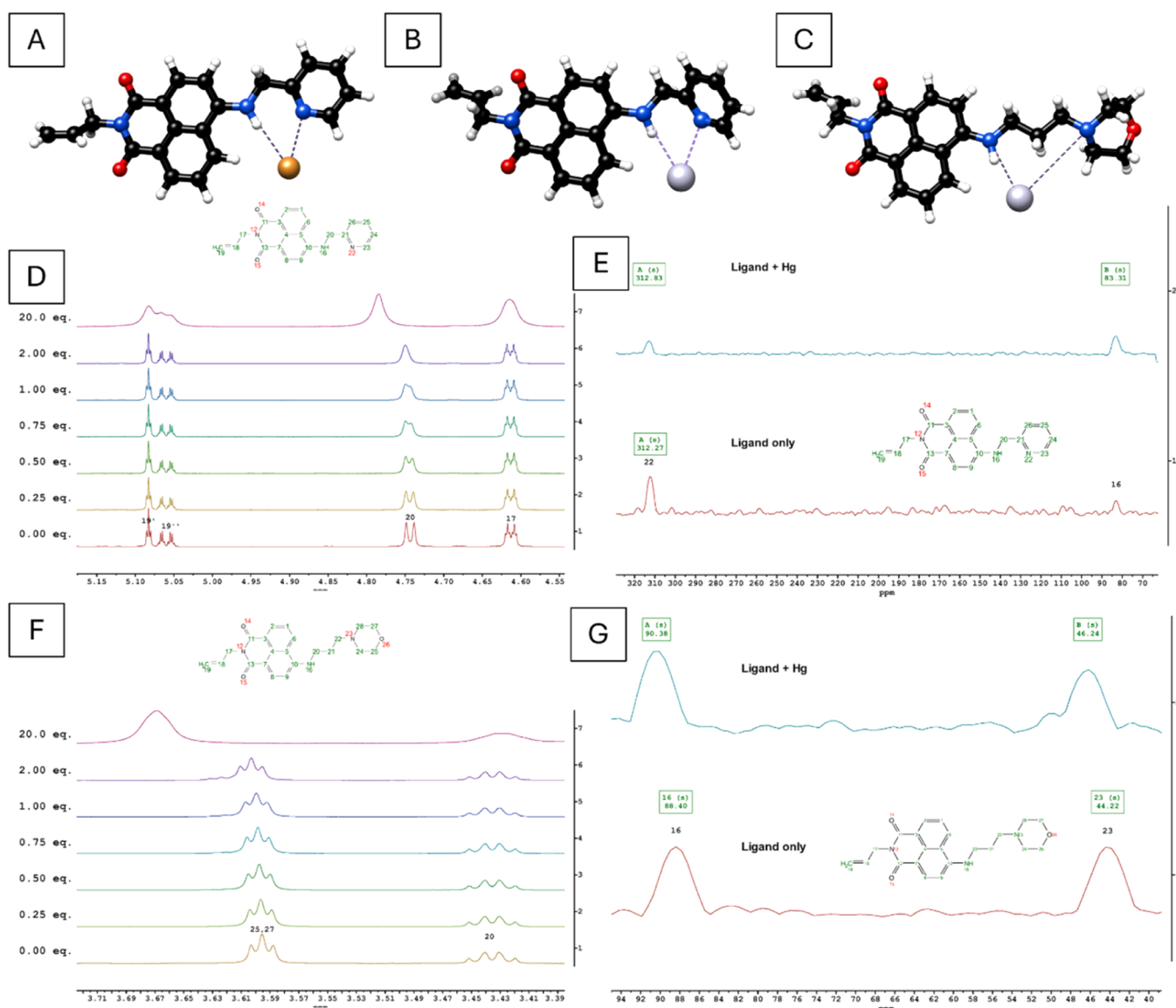


**Fig. 5.** Optimized geometries obtained from DFT calculations from the ORCA 6.0 software: (A) C1-Cu complex; (B) C1-Hg complex; (C) C2-Hg complex. Golden sphere is representative of a Cu<sup>2+</sup> ion and grey sphere is representative of a Hg<sup>2+</sup> metal ion. (D) <sup>1</sup>H NMR titration of compound C1 with increasing additions of Hg<sup>2+</sup> metal ions; (E) <sup>15</sup>N NMR spectra of the free compound C1 and of the C1-Hg complex; (F) <sup>1</sup>H NMR titration of compound C2 with increasing additions of Hg<sup>2+</sup> metal ions; (G) <sup>15</sup>N NMR spectra of the free C2 complex and of the C2-Hg complex.

46.24 ppm and 88.4 ppm to 90.38 ppm, for the morpholine fragment N-atom and linker N-atom respectively. The role of the nitrogen atoms in the complexation mechanisms had also been verified by the theoretical calculations performed. Geometry optimization was obtained from DFT calculations using the BP86 functional, based on the Becke exchange and Perdew correlation. These demonstrate clearly the preferential lowest energy complexation mechanism through the interaction of the Hg<sup>2+</sup> metal ion with both nitrogen atoms in the structure of the compound C1.

A similar approach was conducted for compound C2. Once again, a significant broadening of the peaks was observed, indicating the occurrence of complexation. No alterations were observed in the allyl fragment, similar to what was verified for the compound C1. As seen in Fig. 5F, the major shifts account for the NH group, shifting from 3.60 ppm to 3.67 ppm, indicating the major role of this atom in the complexation mechanism. Moreover, the two CH<sub>2</sub> groups of the morpholine moiety next to the nitrogen atom also had significant shifts from 2.38 to 2.53 ppm, as well as the couple of CH<sub>2</sub> groups closer to the oxygen atom of the morpholine heterocycle which shifted from 3.59 to 3.67 ppm. Similarly to what was verified for the C1 compound, both

nitrogen atoms present in the structure play a crucial role in the molecule's complexation with metal ions. Also, from the <sup>15</sup>N NMR spectra, slight shifts also occurred, namely a 44.22 ppm to 46.24 ppm corresponding to the morpholine fragment N-atom and 88.40 ppm to 90.38 ppm, corresponding to the linker N-atom, as seen in Fig. 5G. This dependence on nitrogen atoms for the complexation mechanism was also verified through the computational calculations, which demonstrated a clear preference in geometry for a structure that allows these interactions as seen in Fig. 5C.

Regarding the compound C3, an <sup>1</sup>H NMR titration was also performed (Figure SI19–20), however only small alterations were observed, possibly due to the lower association constant as calculated from the UV-Vis and fluorometric titrations.

### 3.5. Naphthalimide-doped polymers assessment for environmental detection of heavy metals

To produce a biodegradable, eco-friendly, and cost-effective probe for environmental applications, the sensing capacity of the compounds

(C1, C2, and C3) doped into a Starch polymer was tested for  $\text{Hg}^{2+}$  detection in an aqueous solution. Among the tested polymers, the Starch polymer doped with compound C2 was selected as the best candidate for this application owing to its selectivity for  $\text{Hg}^{2+}$  metal ions. It also demonstrated a clear colorimetric alteration when exposed to increasing metal concentrations (Fig. 6).

Using Starch as a solid support enabled the detection of metal ions in an aqueous media, overcoming the issue of the compounds' insolubility in water. This approach offers a more straightforward and sustainable method for  $\text{Hg}^{2+}$  ion detection. In a preliminary approach, small, doped polymer squares ( $0.5 \times 0.5 \text{ cm}$ ) were subjected to different  $\text{Hg}^{2+}$  concentrations in water (0, 2, 4, and 10  $\mu\text{M}$ ) for 15 min. After this time, the polymeric matrix lost its structural characteristics, liberating the compound into the aqueous environment. This release facilitated the interactions between the ligand and the metal ions, leading to a fluorescence quenching effect in response to concentrations of  $\text{Hg}^{2+}$  higher than 2  $\mu\text{M}$  (Fig. 5).

This part of the study was expanded by examining a more extensive range of  $\text{Hg}^{2+}$  concentrations. Their emission spectra are shown in Fig. 5C. A decrease in the emission intensity was observed in response to the increasing  $\text{Hg}^{2+}$  concentrations. A linear correlation was found between 0 and 4  $\mu\text{M}$ , which was in accordance with the obtained preliminary results. This linear correlation allowed for the determination of the MDQ and MQA, which were 3 and 28 nM, corresponding to 2 and 14 ppb, respectively.

To verify the applicability of this assay to real water samples, the

same methodology was applied to a tap water sample collected from the laboratory. The results are depicted in Fig. 5C. A similar response was obtained for the tap water sample, with a decrease in emission intensity with increasing  $\text{Hg}^{2+}$  concentrations. A linear correlation was also achieved for this sample for concentrations between 0 and 4 nM, and the MDQ and MQA were 23 and 30 nM, respectively, corresponding to 12 and 15 ppb.

For  $\text{Hg}^{2+}$  detection in real water samples, our polymers demonstrated lower and more competitive detection limits compared to other literature data on fluorescent probes, displaying values of 39.2 nM, 160 nM, or 124.3 nM [71–74]. Moreover, our values aligned with those reported by the WHO standards for drinking water, which were 22 nM [75].

Compared to other methods, which may involve more complex and costly materials or procedures, the utilization of Starch-doped polymers as a probe for  $\text{Hg}^{2+}$  detection in aqueous environments is a more sustainable, practical, and accessible alternative with minimal environmental impact. These polymers are also a promising platform for the incorporation of other organic molecules with different sensing capabilities, increasing their stability in aqueous environments and allowing for colorimetric/fluorometric detection of hazardous pollutants.

### 3.6. Antibacterial activity assessment

To further explore the characteristics of the studied compounds, their antibacterial activity was evaluated. Both liquid and solid support-based

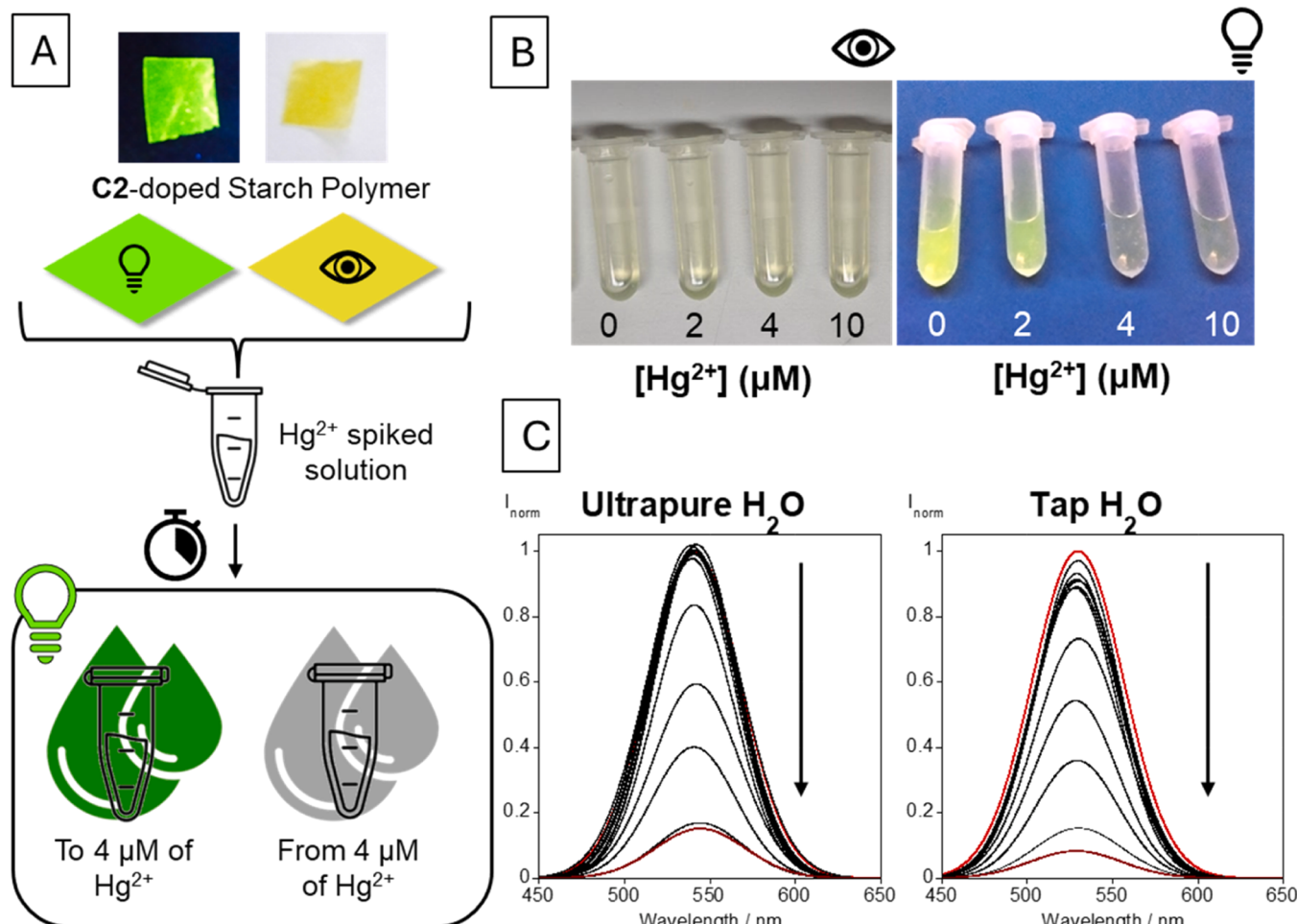


**Fig. 6.** (A) General overview of the workings of the C2 doped Starch polymers for  $\text{Hg}^{2+}$  sensing in water. (B) Naked-eye and Fluorometric alterations under a UV-lamp of C2 doped Starch polymer, in aqueous solutions containing 0, 2, 4, and 10  $\mu\text{M}$  of  $\text{Hg}^{2+}$ . (C) Spectrofluorimetric titrations of the obtained lixiviate of compound C2 in ultrapure and tap water with increased additions of  $\text{Hg}^{2+}$  metal ions,  $\lambda_{\text{exc}} = 435 \text{ nm}$ ,  $T = 25^\circ\text{C}$ .

antibacterial assays were performed to fully assess the antibacterial activity of the compounds and the obtained compound-doped polymers. As for the liquid assessment of the compound's inhibitory activity, broth microdilution assays were performed to evaluate the antibacterial activity of all synthesized compounds. Briefly, a known concentration of bacteria was incubated in the presence of the compounds, with a sample concentration ranging from 0.76 to 0.0015 µg/mL. Gram-negative *Escherichia coli* (E. coli, ATCC® 25922™) and *Pseudomonas aeruginosa* (ATCC ® 9027™) were tested. For Gram-positive bacteria, *Staphylococcus aureus* (ATCC® 6538™), methicillin-resistant *Staphylococcus aureus* (MRSA) (ATCC® 33591™), and *Enterococcus faecalis* (ATCC® 29212™) were examined. These strains were selected due to their relevance when considering increased antimicrobial resistance[76]. *E. coli* or *E. faecalis* are found in natural environments such as water bodies, whereas the remaining strains are found in nosocomial environments and are common causes of bacterial infections in clinical settings.

**Fig. 7** depicts the results obtained through the broth microdilution protocol performed to assess liquid-state antibacterial activity.

All compounds revealed significant antibacterial activity against all tested strains, demonstrating the versatility of the naphthalimide-based compounds as broad-spectrum antibacterial agents. Reports have suggested that the main mechanism by which naphthalimides exhibit a bioactive behavior, correlating with their antibacterial activity, is mostly due to their DNA-binding behavior [77]. This interaction hinders the normal processes of transcription and replication, destabilizing cellular processes and inducing cell death. Moreover, naphthalimides can interact with topoisomerases, inhibiting their interaction with DNA, thus blocking the corrective activity performed by this enzyme [78]. A combination of these two main mechanisms confers an inherent bioactive profile that can be exploited to produce compounds with antibacterial activity. The addition of different substituents, producing naphthalimide-based molecules, can also affect their antibacterial activity, as the added moieties can exhibit antibacterial activity by themselves, inducing synergistic effects and producing a compound with an even higher efficacy regarding its antibacterial effects [79].

A comparative analysis of the inhibitory activity of compounds C1, C2, and C3 was performed through a comparison of their respective Minimum Inhibitory Concentration (MIC) values. For the purposes of our current work, MIC is a reduction higher than 50 % of bacterial growth compared to a bacterial control. **Fig. 6** shows the determined values for all bacterial strains tested. All compounds gave preferential inhibitory activity for the tested Gram-positive strains, particularly against *S. aureus*, for which the lowest MIC values were obtained, 0.05, 0.01 and 0.01 µg/mL for C1, C2, and C3, respectively. Although all compounds produced inhibitory activity for Gram-negative strains, they occurred at higher concentrations compared to the Gram-positive strains. This differential inhibitory response may be related to the more prevalent resistance mechanisms that occur in Gram-negative strains, such as the increased presence of efflux pumps and the presence of a hydrophobic outer membrane [80,81]. The combination of these two factors indicates that Gram-negative strains are harder to inhibit. Nonetheless, considering the difficult development of inhibitory mechanisms for Gram-negative strains, the studied compounds were highly effective, and could act as the basis for the development of other novel, more specific antibacterial compounds.

All studied compounds produced a significant antibacterial activity, against all tested strains, at concentrations that were highly competitive against those reported in the literature for other naphthalimide-based molecules. For example, the literature shows MIC values of 4–16 µg/mL [79] for other naphthalimide-based molecules for the same bacterial strains, whereas our compounds (C1, C2, and C3) produced a similar inhibitory activity at concentrations of 0.38 and 0.76 µg/mL. Similar effects were determined for all tested strains, with reported MICs in the literature of 4 µg/mL for *S. aureus* and MRSA, [79], 31–62 µg/mL for *E. faecalis* and 125–250 µg/mL for *P. aeruginosa* [16], values indicative

of the competitive nature of the herein studied compounds regarding their antibacterial activity.

Overall, the best inhibitory results were consistent with the higher lipophilicity presented by the compounds, as verified by its increased logP value of 3.32 of compound C1, compared to those obtained for compounds C2 and C3 (1.52 and 2.46, respectively). It is important to note that compounds C1 and C2 were effective against MRSA, at a considerably low concentration of 0.38 µg/mL, considering those reported in the literature, and the extensive resistance mechanisms of MRSA.

Following the promising results obtained in the liquid assays, antibacterial assays for the naphthalimide-doped polymers were also performed. In accordance with the results obtained for the liquid assays, the naphthalimide-doped polymers produced a significant antibacterial activity for all tested strains.

As for PVC and PMMMA polymers, the control non-doped polymers produced some contact inhibitory activity, with the occurrence of a slight bacterial growth beneath the surface of the polymers. However, upon the application of the naphthalimide-doped polymers, no growth was detected in the polymer-agar interface. As such, a synergistic interaction may occur between the polymeric matrix and the doped compounds. As the non-doped polymer had already inhibited bacterial growth to a certain degree, the junction of the highly antibacterial compounds in its tri-dimensional structure would increase the efficacy with which the materials produced antibacterial activity.

Conversely, for the obtained Starch polymers, no inhibitory activity was observed for the non-doped control polymers, confirming the biocompatibility of the polymers. As the polymers were produced using an aqueous environment, without the presence of toxic chemical agents, we expected that the bacteria would not be susceptible to this control material. Upon the application of the compounds onto the polymers, a strong inhibitory activity was observed for all bacterial strains, corroborating the effects already determined through the liquid assays.

**Fig. 8** exemplifies the results achieved with Gram-negative bacteria, *E. coli*, and Gram-positive bacteria, MRSA, showing the wide-ranging antibacterial efficacy of these polymers. The remaining results are depicted in the [Supplementary Material](#) (Figure SI21). As no halos were observed for any of the polymers, all inhibitory activity occurred through direct contact inhibition, without compound diffusion to the medium.

The results highlighted the strong inhibitory influence of the naphthalimide-doped polymers against Gram-positive and Gram-negative bacteria. From the diverse polymeric matrices utilized, a wide range of applications are possible. Due to the widespread usage of PVC and PMMMA materials in society, high-risk zones for bacterial contamination, as high-contact surfaces, could be either coated or produced using these materials, introducing a new level of security against bacterial contaminations. Moreover, the use of a biocompatible and sustainable Starch-based material also provides another alternative to conventional petrochemical-based polymeric matrices for food packaging, surface coatings, etc. Although more studies are needed to further optimize the production of such materials, perhaps in a scaled-up version, the results obtained herein highlight the concept for possible future applications.

### 3.7. Environmental impact assessment

An important aspect to consider, when handling polymeric matrices is their environmental impact. The studied materials are no exception, particularly when considering the Starch C2 doped polymer, and its sensing activity for aqueous environments. This polymer was selected to evaluate its environmental impact, due to its multifunctionality, acting not only as an antibacterial surface but also as a mercury sensor. Although the synthetic route of this polymer is already environmentally friendly, additional tests were conducted to further confirm the environmental impact of the obtained material in a real-life practical

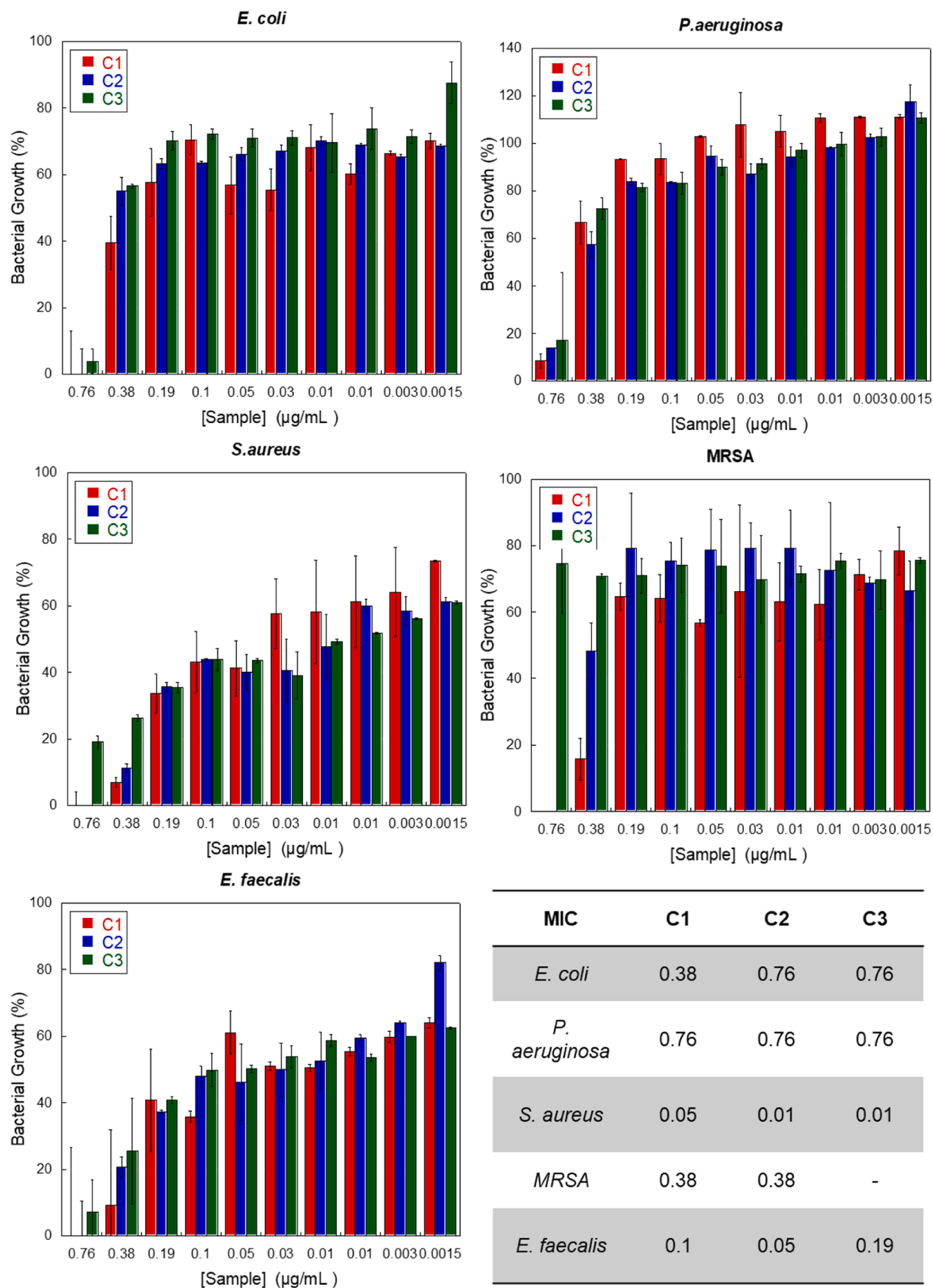
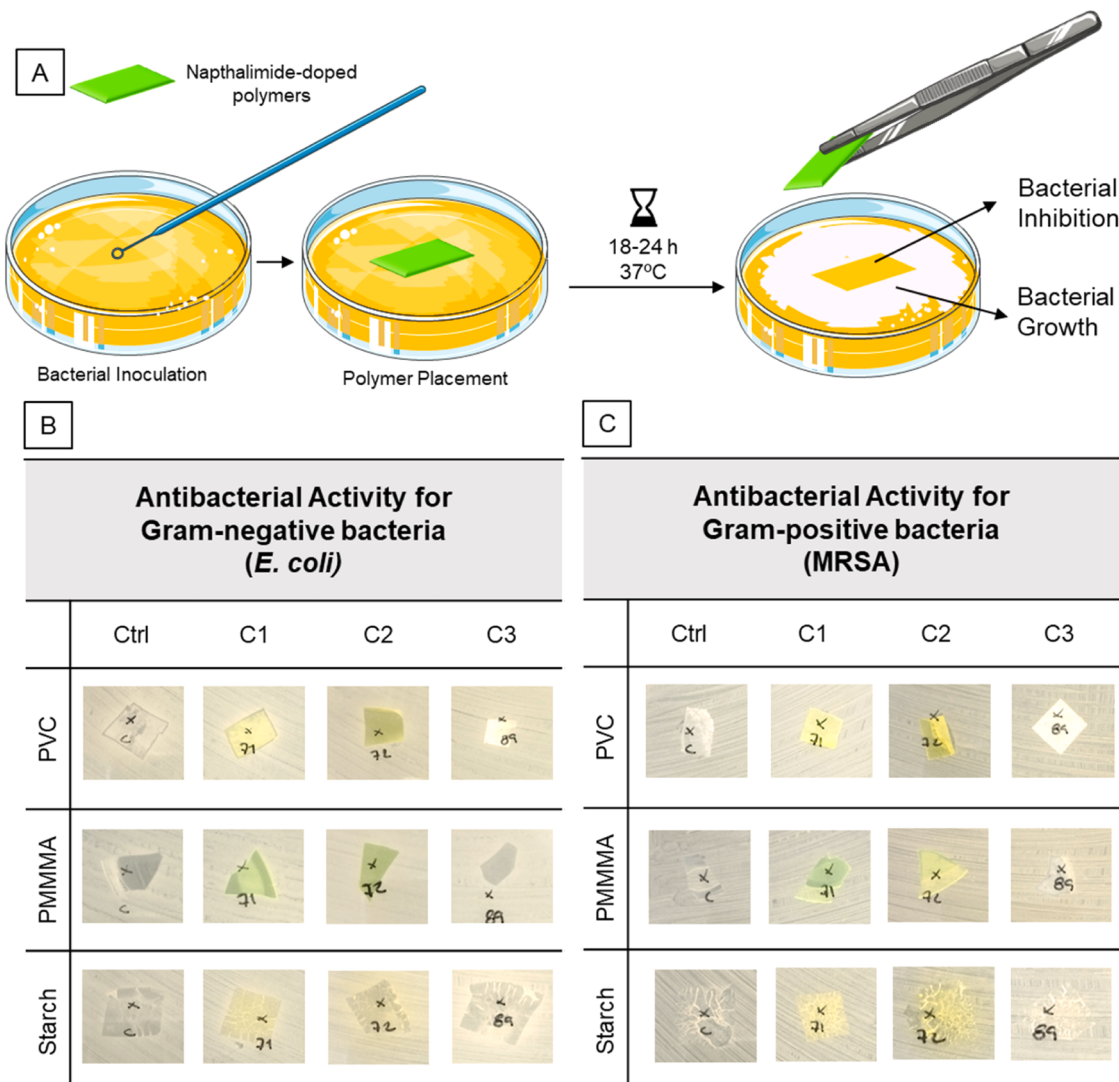


Fig. 7. Bacterial Growth Profiles for all tested bacterial strains. Minimum Inhibitory Concentrations (MIC) are depicted as compound concentrations in  $\mu\text{g/mL}$ .



**Fig. 8.** Schematic Overview of the antibacterial activity presented by polymers doped with compounds C1, C2 and C3 (A). Polymeric Antibacterial Activity for polymers doped with compounds C1, C2 and C3 against *E. coli* (B) and MRSA (C).

situation.

To this end, five 1 cm<sup>2</sup> squares of the polymer were submerged in 10 mL of water and left until complete dissolution of the polymer was obtained, and the resulting lixiviate was suitable for analysis. This step guaranteed the full release of the compound in the polymeric matrix to the aqueous environment, which consisted of an approximate mass of 0.025 mg per square, yielding a total mass of 0.125 mg of compound released into the solution.

To evaluate the environmental impact of the obtained lixiviate, the Microtox® assay was employed. This assay is based on the bioluminescent behavior of *Vibrio fischeri* and is one of the most versatile and sensitive tests for toxicity evaluation, where it is used in a variety of matrices and samples [82–84]. Moreover, its nature allows for the assessment of various samples in a single assay, and it has no associated ethical issues, as the assay is conducted using a bacterial strain [85]. *V. fischeri* is commonly found in marine environments and inherently contains the luciferase enzyme, which catalyzes the oxidation of their substrate, luciferin, in a process mediated by a reduced coenzyme, flavin mononucleotide [86]. In the presence of a compound with toxic activity, the inherent bioluminescence of the bacteria decreases, allowing for an assessment of the compound's toxicity in only 30 min. As such, when exposed to a specific amount of compound, it allowed for the determination of the EC<sub>50</sub>, a concentration value at which the bioluminescence

decreases by 50 %. Fig. 9 shows a graphical representation of the assay and the results for the lixiviate obtained through the solubilization of the C2-doped Starch polymer, after 15 and 30 min.

The % Effect was calculated as the percentage of luminescence intensity produced in response to that specific concentration at a determined time point. The lixiviate produced a maximum effect of 18.52 ± 0.14 % and 18.9 ± 0.7 % for the maximum concentration, after 15 and 30 min. This decrease was insufficient to produce a 50 % decrease in bioluminescence and the subsequent determination of an EC<sub>50</sub>. As such, this material did not possess a significant environmental toxicity. Moreover, as the polymeric matrix was composed solely of Starch and water, it should not present any inherent toxicity to the environment, further confirming this material's non-toxicity and sustainable nature for a low-cost, environmentally friendly sensor with inherent antibacterial properties.

#### 4. Conclusions

In short, the development of naphthalimide-based compounds and their integration into various polymeric matrices was a highly effective strategy for addressing critical environmental and health safety concerns. Three naphthalimide derivatives (C1, C2, and C3) were successfully synthesized and characterized in both liquid and solid state,

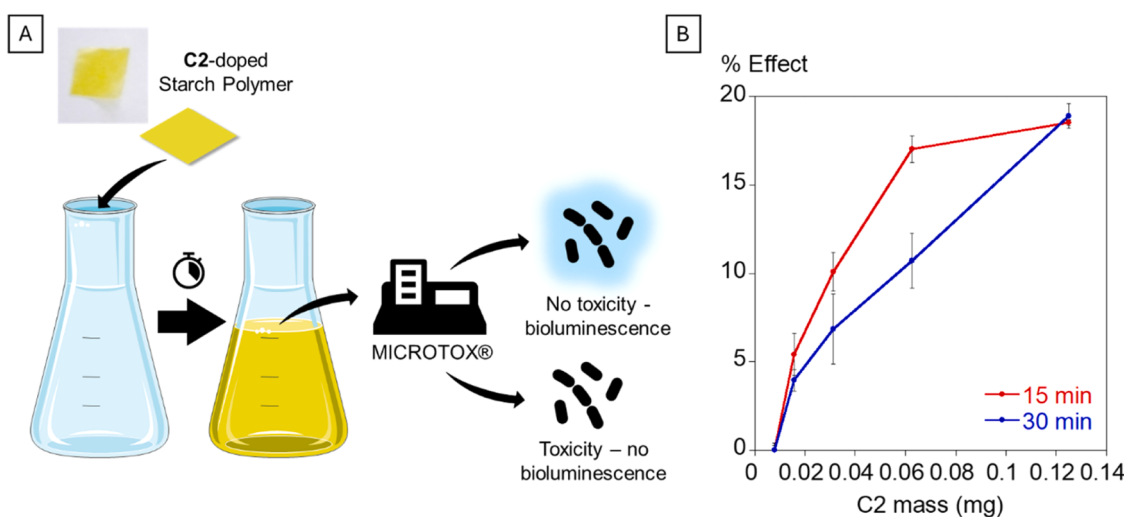


Fig. 9. Schematic Overview of the MICROTOX® Assay (A) Mass-response curve obtained for the C2 doped Starch lixiviate polymer in the Microtox® Assay (B).

demonstrating their potential as fluorometric sensors for  $Hg^{2+}$  detection and as antibacterial agents. Compound C2 showed a strong and selective affinity for  $Hg^{2+}$  in the liquid state. Furthermore, these compounds were encapsulated in PVC, PMMMA and Starch matrices. The C2-Starch doped polymer offered a novel, cost-effective, sustainable approach for  $Hg^{2+}$  detection in aqueous environments, with a visual limit of detection of 4  $\mu M$  (2 ppm), and a spectroscopical MDQ of 3 nM (2 ppb). In real water samples, the MDQ was 23 nM (12 ppb). The MICROTOX® Assay confirmed the non-toxic nature of the C2-Starch polymer, aligning with green chemistry principles.

Additionally, the antibacterial activity observed in both solution and solid forms against resistant strains highlights the dual utility of these materials for environmental monitoring and as antimicrobial surfaces or coatings. They showed competitive MIC against *S. aureus*, ( $MIC_{50} = 0.05\text{--}0.1 \mu g/mL$ ) and effectively hindered bacterial growth of MRSA.

These findings open potential applications for the development of antibacterial surfaces for clinical and industrial applications. Most importantly, they demonstrate the potential of bioplastics as probes for detecting pollutant agents in aqueous environments sustainably, quickly, and cost-effectively.

#### Statement of "Environmental implications"

Mercury ions and antibiotic-resistant bacteria represent a substantial threat to both environmental and human health, due to their bioaccumulation and possible widespread contamination. Mercury, a highly toxic compound, poses a serious risk to aquatic and human health through its bioaccumulation profile. Antibiotic resistant bacteria are yet another risk, with environmental transmission contributing to the ongoing threat of resistant infections. By synthesizing naphthalimide-based compounds, and incorporating them in solid support matrixes, this work provides a sustainable, green-chemistry oriented dual solution, producing a material with high selectivity for the detection of mercury, while simultaneously demonstrating potent antibacterial properties.

#### Author contributions

J.G. contributed to the methodology, experiment, investigation and data analysis; E.O. contributed to the conceptualization, investigation, data analysis, experiment, resources, project management, supervision, methodology, and funding acquisition; H.M.S. contributed to the investigation (mass spectra studies), resources and funding acquisition; J.L.C.M. contributed to resources and funding acquisition; C.L.

contributed to methodology, data analysis, resources, supervision and funding acquisition; P.M.P.D. contributed to the investigation, resources and data analysis; G.D. contributed to the conceptualization, investigation, data analysis, experiment, resources, methodology, and funding acquisition; A.K. contributed to the conceptualization, investigation, experiment, data analysis, experiment, resources, methodology, supervision, project management, and funding acquisition.

The manuscript was written through the contributions of all authors. All authors approved the final version of the manuscript.

#### CRediT authorship contribution statement

**Elisabete De Jesus Oliveira:** Writing – review & editing, Writing – original draft, Validation, Supervision, Resources, Project administration, Methodology, Investigation, Funding acquisition, Formal analysis, Conceptualization. **Carlos Lodeiro:** Writing – review & editing, Writing – original draft, Validation, Supervision, Resources, Methodology, Funding acquisition, Formal analysis. **Jose Luis Capelo-Martínez:** Writing – review & editing, Resources, Funding acquisition. **Hugo M. Santos:** Writing – review & editing, Writing – original draft, Resources, Investigation, Funding acquisition. **Joana Galhano:** Writing – review & editing, Writing – original draft, Methodology, Investigation, Formal analysis. **Georgi M. Dobrikov:** Writing – review & editing, Writing – original draft, Resources, Methodology, Investigation, Funding acquisition, Formal analysis, Conceptualization. **Atanas Kurutos:** Writing – review & editing, Writing – original draft, Validation, Resources, Methodology, Investigation, Funding acquisition, Formal analysis, Conceptualization. **Maria Paula Duarte:** Writing – review & editing, Resources, Investigation, Formal analysis.

#### Declaration of Competing Interest

The authors declare that they have no known competing financial interests or personal relationships that could have appeared to influence the work reported in this paper.

#### Acknowledgements

This work was supported by the Associate Laboratory for Green Chemistry - LAQV which is financed by national funds from FCT/MCTES (LA/P/0008/2020 DOI 10.54499/LA/P/0008/2020, UIDP/50006/2020 DOI 10.54499/UIDP/50006/2020 and UIDB/50006/2020 DOI 10.54499/UIDB/50006/2020) as well as the Scientific Society

PROTEOMASS (Portugal) for funding support (General Funding Grant 2023–2024). J.G. thanks FCT/MEC (Portugal) for her doctoral grant 2022.09495. BD†. E.O thanks FCT/MEC (Portugal) for the individual contract, CEECIND/05280/2022. HMS acknowledges the Associate Laboratory for Green Chemistry-LAQV (LA/P/0008/2020) funded by FCT/MCTES for his research contract.

The financial support by the Bulgarian National Science Fund (BNSF) under grant – "Novel styryl and polymethine fluorophores as potential theranostic agents" contract KP-06-M59/1 from 15.11.2021 is gratefully acknowledged by A.K. This work is also developed, funded, and acknowledged by A.K. as part of by European Union-NextGenerationEU, through the National Recovery and Resilience Plan of the Republic of Bulgaria, project No BG-RRP-2.004–0002, "BiOrgaMCT. G.D. thanks to the European Regional Development Fund within the Operational Programme Science and Education for Smart Growth 2014–2020 under the Project Center of Excellence: National center of mechatronics and clean technologies - BG05M2OP001–1.001-0008 for the financial support.

## Appendix A. Supporting information

Supplementary data associated with this article can be found in the online version at [doi:10.1016/j.jhazmat.2024.136107](https://doi.org/10.1016/j.jhazmat.2024.136107).

## Data Availability

Data will be made available on request.

## References

- [1] Ye, Q., Ren, S., Huang, H., Duan, G., Liu, K., Liu, J.-B., 2020. Fluorescent and colorimetric sensors based on the oxidation of o-phenylenediamine. *ACS Omega* 5, 20698–20706. <https://doi.org/10.1021/acsomega.0c03111>.
- [2] Wu, Y., Feng, J., Hu, G., Zhang, E., Yu, H.-H., 2023. Colorimetric sensors for chemical and biological sensing applications. *Sensors* 23, 2749. <https://doi.org/10.3390/s23052749>.
- [3] Tchounwou, P.B., Yedjou, C.G., Patlolla, A.K., Sutton, D.J., 2012. In: Luch, A. (Ed.), Heavy Metal Toxicity and The Environment. Springer, Basel, pp. 133–164. [https://doi.org/10.1007/978-3-7643-8340-4\\_6](https://doi.org/10.1007/978-3-7643-8340-4_6).
- [4] Hama Aziz, K.H., Mustafa, F.S., Omer, K.M., Hama, S., Hamarawf, R.F., Rahman, K. O., 2023. Heavy metal pollution in the aquatic environment: efficient and low-cost removal approaches to eliminate their toxicity: a review. *RSC Adv* 13, 17595–17610. <https://doi.org/10.1039/D3RA00723E>.
- [5] 10 chemicals of public health concern, (n.d.). (<https://www.who.int/news-room/photo-story/photo-story-detail/10-chemicals-of-public-health-concern>) (accessed July 19, 2024).
- [6] Basu, N., Bastiansz, A., Dórea, J.G., Fujimura, M., Horvat, M., Shroff, E., et al., 2023. Our evolved understanding of the human health risks of mercury. *Ambio* 52, 877–896. <https://doi.org/10.1007/s13280-023-01831-6>.
- [7] Wei, Q., Nagi, R., Sadeghi, K., Feng, S., Yan, E., Ki, S.J., et al., 2014. Detection and spatial mapping of mercury contamination in water samples using a smart-phone. *ACS Nano* 8, 1121–1129. <https://doi.org/10.1021/mn406571t>.
- [8] Liu, L., Shi, H., Li, R., Liu, C., Cheng, J., Gao, L., 2021. Highly sensitive detection for mercury ions using graphene oxide (GO) sensors. *Micro (Basel)* 12, 1070. <https://doi.org/10.3390/mi12091070>.
- [9] Gao, L., Lv, Q., Xia, N., Lin, Y., Lin, F., Han, B., 2021. Detection of mercury ion with high sensitivity and selectivity using a DNA/graphene oxide hybrid immobilized on glass slides. *Biosens (Basel)* 11, 300. <https://doi.org/10.3390/bios11090300>.
- [10] Wang, Y., Zhang, L., Han, X., Zhang, L., Wang, X., Chen, L., 2021. Fluorescent probe for mercury ion imaging analysis: strategies and applications. *Chem Eng J* 406, 127166. <https://doi.org/10.1016/j.cej.2020.127166>.
- [11] Li, G., Wang, J., Li, D., Liu, S., Yin, J., Lai, Z., et al., 2021. A Hg(II)-specific probe for imaging application in living systems and quantitative analysis in environmental/food samples. *Chin Chem Lett* 32, 1527–1531. <https://doi.org/10.1016/j.clet.2020.09.040>.
- [12] Cheng, X., Huang, S., Lei, Q., Chen, F., Zheng, F., Zhong, S., et al., 2022. The exquisite integration of ESIPT, PET and AIE for constructing fluorescent probe for Hg(II) detection and poisoning. *Chin Chem Lett* 33, 1861–1864. <https://doi.org/10.1016/j.clet.2021.10.024>.
- [13] Fan, M., Pan, Z., Wang, C., Guo, Y., Sun, J., Liu, M., et al., 2022. Quantitative visual detection of mercury ions with ratiometric fluorescent test paper sensor. *Front Chem* 10, 859379. <https://doi.org/10.3389/fchem.2022.859379>.
- [14] Duke, R.M., Veale, E.B., Pfeffer, F.M., Kruger, P.E., Gunnlaugsson, T., 2010. Colorimetric and fluorescent anion sensors: an overview of recent developments in the use of 1,8-naphthalimide-based chemosensors. *Chem Soc Rev* 39, 3936. <https://doi.org/10.1039/b910560n>.
- [15] Lei, S., Meng, X., Wang, L., Zhou, J., Qin, D., Duan, H., 2021. A naphthalimide-based fluorescent probe for the detection and imaging of mercury ions in living cells. *ChemistryOpen* 10, 1116–1122. <https://doi.org/10.1002/open.202100204>.
- [16] Su, M., Liu, C., Liang, Y., Zhang, Y., Rong, X., Wang, X., et al., 2022. A novel water-soluble naphthalimide-based turn-on fluorescent probe for mercury ion detection in living cells and zebrafish. *N J Chem* 46, 10951–10956. <https://doi.org/10.1039/D2NJ01314B>.
- [17] Said, A.I., Staneva, D., Angelova, S., Grabchev, I., 2022. Self-associated 1,8-naphthalimide as a selective fluorescent chemosensor for detection of high pH in aqueous solutions and their Hg<sup>2+</sup> contamination. *Sensors* 23, 399. <https://doi.org/10.3390/s23010399>.
- [18] Choi, S.-A., Park, C.S., Kwon, O.S., Giorgi, H.-K., Lee, J.-S., Ha, T.H., et al., 2016. Structural effects of naphthalimide-based fluorescent sensor for hydrogen sulfide and imaging in live zebrafish. *Sci Rep* 6, 26203. <https://doi.org/10.1038/srep26203>.
- [19] Kamal, A., Bolla, N.R., Srikanth, P.S., Srivastava, A.K., 2013. Naphthalimide derivatives with therapeutic characteristics: a patent review. *Expert Opin Ther Pat* 23, 299–317. <https://doi.org/10.1517/13543776.2013.746313>.
- [20] Korycka-Machala, M., Nowosielski, M., Kuron, A., Rykowski, S., Olejniczak, A., Hofmann, M., et al., 2017. Naphthalimides selectively inhibit the activity of bacterial, replicative DNA ligases and display bactericidal effects against Tubercle Bacilli. *Molecules* 22, 154. <https://doi.org/10.3390/molecules22010154>.
- [21] Duke, R.M., Veale, E.B., Pfeffer, F.M., Kruger, P.E., Gunnlaugsson, T., 2010. Colorimetric and fluorescent anion sensors: an overview of recent developments in the use of 1,8-naphthalimide-based chemosensors. *Chem Soc Rev* 39, 3936. <https://doi.org/10.1039/b910560n>.
- [22] Niu, C.-G., Qin, P.-Z., Zeng, G.-M., Gui, X.-Q., Guan, A.-L., 2007. Fluorescence sensor for water in organic solvents prepared from covalent immobilization of 4-morpholinyl-1,8-naphthalimide. *Anal Bioanal Chem* 387, 1067–1074. <https://doi.org/10.1007/s00216-006-1016-y>.
- [23] Georgiev, N.I., Krasteva, P.V., Bakov, V.V., Bojinov, V.B., 2022. A highly water-soluble and solid state emissive 1,8-naphthalimide as a fluorescent PET probe for determination of pHs, Acid/base vapors, and water content in organic solvents. *Molecules* 27, 4229. <https://doi.org/10.3390/molecules27134229>.
- [24] Xu, Z., Zhou, Y., Wang, J., Mao, L., Li, W., Xu, G., 2021. The synthesis and antitumor activity of 1,8-naphthalimide derivatives linked 1,2,3-triazole. *Front Bioeng Biotechnol* 9. <https://doi.org/10.3389/fbioe.2021.662432>.
- [25] de Oliveira, K.N., Costa, P., Santin, J.R., Mazzambani, L., Bürger, C., Mora, C., et al., 2011. Synthesis and antidepressant-like activity evaluation of sulphonamides and sulphonyl-hydrazones. *Bioorg Med Chem* 19, 4295–4306. <https://doi.org/10.1016/j.bmc.2011.05.056>.
- [26] Kumar, S., Muhammed, S., Alarfaji, S.S., Yoon, S., Kim, M., Youm, K., et al., 2021. Experimental and computational study of naphthalimide derivatives: synthesis, optical, nonlinear optical and antiviral properties. *Opt (Stuttgart)* 246, 167748. <https://doi.org/10.1016/j.ijleo.2021.167748>.
- [27] Carretero, G.P.B., Saraiva, G.K.V., Rodrigues, M.A., Kiyota, S., Bemquerer, M.P., Chaimovich, H., et al., 2021. Naphthalimide-containing BP100 leads to higher model membranes interactions and antimicrobial activity. *Biomolecules* 11, 542. <https://doi.org/10.3390/biom11040542>.
- [28] Shao, J., Li, Y., Wang, Z., Xiao, M., Yin, P., Lu, Y., et al., 2013. 7b, a novel naphthalimide derivative, exhibited anti-inflammatory effects via targeted-inhibiting TAK1 following down-regulation of ERK1/2- and p38 MAPK-mediated activation of NF-κB in LPS-stimulated RAW264.7 macrophages. *Int Immunopharmacol* 17, 216–228. <https://doi.org/10.1016/j.intimp.2013.06.008>.
- [29] Shalini, M.D., Johansen, L., Kremer, V., Kumar, 2019. Variedly connected 1,8-naphthalimide-7-chloroquinoline conjugates: Synthesis, anti-mycobacterial and cytotoxic evaluation. *Bioorg Chem* 92, 103241. <https://doi.org/10.1016/j.bioorg.2019.103241>.
- [30] Ippili, S., Jung, J.-S., Thomas, A.M., Vuong, V.-H., Lee, J.-M., Sha, M.S., et al., 2023. An overview of polymer composite films for antibacterial display coatings and sensor applications. *Polym (Basel)* 15, 3791. <https://doi.org/10.3390/polym15183791>.
- [31] Lewandowski, K., Skórczewska, K., 2022. A brief review of poly(vinyl chloride) (PVC) recycling. *Polym (Basel)* 14, 3035. <https://doi.org/10.3390/polym14153035>.
- [32] Lebeau, J., Efrosman, J.P., Lynch, M.D., 2020. A review of the biotechnological production of methacrylic acid. *Front Bioeng Biotechnol* 8. <https://doi.org/10.3389/fbioe.2020.00207>.
- [33] Braun, D., 2004. Poly(vinyl chloride) on the way from the 19th century to the 21st century. *J Polym Sci A Polym Chem* 42, 578–586. <https://doi.org/10.1002/pola.10906>.
- [34] Bergthaller, W., Hollmann, J., 2014. Starch, in: Reference Module in Chemistry, Molecular Sciences and Chemical Engineering, Elsevier, 2014. <https://doi.org/10.1016/B978-0-12-409547-2.11374-5>.
- [35] Neese, F., 2000. An improvement of the resolution of the identity approximation for the formation of the Coulomb matrix. *J Comput Chem* 24, 1740–1747. <https://doi.org/10.1002/jcc.10318>.
- [36] Neese, F., 2000. Approximate second-order SCF convergence for spin unrestricted wavefunctions. *Chem Phys Lett* 93–98. [https://doi.org/10.1016/S0009-2614\(00\)00662-X](https://doi.org/10.1016/S0009-2614(00)00662-X).
- [37] Neese, F., Wennmohs, F., Becker, U., Ripplinger, C., 2020. The ORCA quantum chemistry program package. *J Chem Phys* 152, 224108. <https://doi.org/10.1063/5.0004608>.
- [38] Neese, F., 2018. Software update: the ORCA program system, version 4.0. *WIREs Comput Mol Sci* 8. <https://doi.org/10.1002/wcms.1327>.

- [39] Neese, F., 2012. The ORCA program system. *WIREs Comput Mol Sci* 2, 73–78. <https://doi.org/10.1002/wcms.81>.
- [40] Neese, F., 2023. The SHARK integral generation and digestion system. *J Comput Chem* 44, 381–396. <https://doi.org/10.1002/jcc.26942>.
- [41] Hanwell, M.D., Curtis, D.E., Lonio, D.C., Vandermeersch, T., Zurek, E., Hutchison, G.R., 2012. Avogadro: an advanced semantic chemical editor, visualization and analysis platform. *J Chemin-* 4, 1–17. <https://doi.org/10.1186/1758-2946-4-17/FIGURES/14>.
- [42] Pettersen, E.F., Goddard, T.D., Huang, C.C., Couch, G.S., Greenblatt, D.M., Meng, E.C., et al., 2004. UCSF Chimera—a visualization system for exploratory research and analysis. *J Comput Chem* 25, 1605–1612. <https://doi.org/10.1002/jcc.20084>.
- [43] Kellogg, R.E., Bennett, R.G., 1964. Radiationless intermolecular energy transfer. III. Determination of phosphorescence efficiencies. *J Chem Phys* 41, 3042–3045. <https://doi.org/10.1063/1.1725672>.
- [44] Reynolds, G.A., Drexhage, K.H., 1975. New coumarin dyes with rigidized structure for flashlamp-pumped dye lasers. *Opt Commun* 13, 222–225. [https://doi.org/10.1016/0030-4018\(75\)90085-1](https://doi.org/10.1016/0030-4018(75)90085-1).
- [45] Pedro, G., Duarte, F., Dobrikov, G.M., Kurutosi, A., Santos, H.M., Capelo-Martínez, J.L., et al., 2024. Optical evaluation of dansyl derivatives and their implementation in low-cost and flexible dye-doped PMMA platforms for efficient detection of hazardous chemical vapours. *Dyes Pigments* 224, 112042. <https://doi.org/10.1016/j.dyepig.2024.112042>.
- [46] Diamantis, S.A., Pournara, A.D., Koutsouroubi, E.D., Mouilaras, C., Deligiannakis, Y., Armatas, G.S., et al., 2022. Detection and sorption of heavy metal ions in aqueous media by a fluorescent Zr(IV) metal–organic framework functionalized with 2-picolyamine receptor groups. *Inorg Chem* 61, 7847–7858. <https://doi.org/10.1021/acs.inorgchem.2c00434>.
- [47] Zhou, S., Zhou, Z.-Q., Zhao, X.-X., Xiao, Y.-H., Xi, G., Liu, J.-T., et al., 2015. A dansyl based fluorescence chemosensor for Hg<sup>2+</sup> and its application in the complicated environment samples. *Spectrochim Acta A Mol Biomol Spectrosc* 148, 348–354. <https://doi.org/10.1016/j.saa.2015.03.126>.
- [48] Gao, T., Huang, X., Huang, S., Dong, J., Yuan, K., Feng, X., et al., 2019. Sensitive water-soluble fluorescent probe based on upolding and aggregation-induced emission strategies for selective detection of Hg<sup>2+</sup> in living cells and zebrafish. *J Agric Food Chem* 67, 2377–2383. <https://doi.org/10.1021/acs.jafc.8b06895>.
- [49] Alaei, P., Rouhani, S., Gharanjig, K., Ghasemi, J., 2012. A new polymerizable fluorescent PET chemosensor of fluoride (F<sup>-</sup>) based on naphthalimidethiourea dye. *Spectrochim Acta A Mol Biomol Spectrosc* 90, 85–92. <https://doi.org/10.1016/j.saa.2012.01.008>.
- [50] Schulz, A., Wotschadlo, J., Heinze, T., Mohr, G.J., 2010. Fluorescent nanoparticles for ratioimetric pH-monitoring in the neutral range. *J Mater Chem* 20, 1475. <https://doi.org/10.1039/b918427a>.
- [51] Huang, G., Li, C., Han, X., Aderinto, S.O., Shen, K., Mao, S., et al., 2018. 2018. Sensitive and selective detection of Cu(II) ion: a new effective 1,8-naphthalimid-based fluorescence ‘turn off’ sensor. *Luminescence* 33, 660–669. <https://doi.org/10.1002/bio.3461>.
- [52] Fang, X., Zhang, Y., Li, M., Zhang, Z., Qi, Y., Zhang, X., et al., 2023. A colorimetric and fluorometric molecular system for discriminative detection of palladium acetate and CO cell imaging. *Dyes Pigments* 209, 110929. <https://doi.org/10.1016/j.dyepig.2022.110929>.
- [53] Fülop, A., Arian, D., Lysenko, A., Mokhir, A., 2009. A simple method for monitoring protein–DNA interactions. *Bioorg Med Chem Lett* 19, 3104–3107. <https://doi.org/10.1016/j.bmcl.2009.03.167>.
- [54] Hanaka, K., Muramatsu, Y., Urano, Y., Terai, T., Nagano, T., 2010. Design and synthesis of a highly sensitive off-on fluorescent chemosensor for zinc ions utilizing internal charge transfer. *Chem – A Eur J* 16, 568–572. <https://doi.org/10.1002/chem.200901591>.
- [55] Biswas, S., Dutta, T., Silswal, A., Bhowal, R., Chopra, D., Koner, A.L., 2021. Strategic engineering of alkyl spacer length for a pH-tolerant lysosome marker and dual organelle localization. *Chem Sci* 12, 9630–9644. <https://doi.org/10.1039/DSC00542A>.
- [56] Zhang, Z., Li, Y., He, H., Qian, X., Yang, Y., 2016. Mild chemotriggered generation of a fluorophore-tethered diazoalkane species via smiles rearrangement. *Org Lett* 18, 4674–4677. <https://doi.org/10.1021/acs.orglett.6b02303>.
- [57] Demets, G.J.-F., Triboni, E.R., Alvarez, E.B., Arantes, G.M., Filho, P.B., Politi, M.J., 2006. Solvent influence on the photophysical properties of 4-methoxy-N-methyl-1,8-naphthalimide. *Spectrochim Acta A Mol Biomol Spectrosc* 63, 220–226. <https://doi.org/10.1016/j.saa.2005.05.008>.
- [58] Nicolescu, A., Airinei, A., Georgescu, E., Georgescu, F., Tigoianu, R., Oancea, F., et al., 2020. Synthesis, photophysical properties and solvatochromic analysis of some naphthalene-1,8-dicarboxylic acid derivatives. *J Mol Liq* 303, 112626. <https://doi.org/10.1016/j.molliq.2020.112626>.
- [59] Dhar, S., Singha Roy, S., Rana, D.K., Bhattacharya, S., Bhattacharya, S., Bhattacharya, S.C., 2011. Tunable solvatochromic response of newly synthesized antioxidative naphthalimide derivatives: intramolecular charge transfer associated with hydrogen bonding effect. *J Phys Chem A* 115, 2216–2224. <https://doi.org/10.1021/jp1117773>.
- [60] Waghorne, W.E., 2020. A study of kamlet–taft  $\beta$  and  $\pi^*$  scales of solvent basicity and polarity/polarizability using computationally derived molecular properties. *J Solut Chem* 49, 466–485. <https://doi.org/10.1007/s10953-020-00979-z>.
- [61] Galhano, J., Kurutosi, A., Dobrikov, G.M., Duarte, M.P., Santos, H.M., Capelo-Martínez, J.L., et al., 2024. Innovative colorimetric detection of clinical Gram-negative bacteria using low-cost bacteriostatic barbiturate polymers. *Mater Today Chem* 36, 101951. <https://doi.org/10.1016/j.mtchem.2024.101951>.
- [62] Xiang, G., Li, J., Han, W., Yang, Y., Lin, Q., Yang, Y., et al., 2022. The influence of temperature changes on the rice starch structure and digestive characteristics: one and two-step annealing. *Foods* 11, 3641. <https://doi.org/10.3390/foods11223641>.
- [63] Paluch, M., Ostrowska, J., Tyński, P., Sadurski, W., Konkol, M., 2022. Structural and thermal properties of starch plasticized with glycerol/urea mixture. *J Polym Environ* 30, 728–740. <https://doi.org/10.1007/s10924-021-02235-x>.
- [64] Nanda, S., Patra, B.R., Patel, R., Bakos, J., Dalai, A.K., 2022. Innovations in applications and prospects of bioplastics and biopolymers: a review. *Environ Chem Lett* 20. <https://doi.org/10.1007/s10311-021-01334-4>.
- [65] Jachak, M., Bhise, R., Chaturvedi, A., Kamble, V., Shankarling, G., 2022. Pyrroloquinoline based styryl dyes doped PMMA, PS, and PS/TiO<sub>2</sub> polymer for fluorescent applications. *J Inorg Organomet Polym Mater* 32, 2441–2454. <https://doi.org/10.1007/s10904-022-02285-1>.
- [66] Erbaş, S.Ç., Uregil, U., Güle, S., Bastürk, S.B., 2020. Investigation of spectroscopic and thermo-mechanical behaviors of different phenanthroimidazole-azo dyes in solvent and polymer medium. *Mater Res Express* 7, 035101. <https://doi.org/10.1088/2053-1591/ab7c24>.
- [67] Teixeira Alves Duarte, L.G., Coelho, F.L., Germino, J.C., Gamino da Costa, G., Berbigier, J.F., Rodembusch, F.S., et al., 2020. A selective proton transfer optical sensor for copper II based on chelation enhancement quenching effect (CHEQ). *Dyes Pigments* 181, 108566. <https://doi.org/10.1016/j.dyepig.2020.108566>.
- [68] Doerr, L.H., Del Rosario, C., Fan, A., 2023. Metallophilic interactions. in: *Comprehensive Inorganic Chemistry III*. Elsevier, pp. 665–739. <https://doi.org/10.1016/B978-0-12-823144-9.00171-0>.
- [69] Gans, P., Sabatini, A., Vacca, A., 1996. Investigation of equilibria in solution. Determination of equilibrium constants with the HYPERQUAD suite of programs. *Talanta* 43. [https://doi.org/10.1016/0039-9140\(96\)01958-3](https://doi.org/10.1016/0039-9140(96)01958-3).
- [70] Gans, P., Sabatini, A., Vacca, A., 1999. Determination of equilibrium constants from spectrophotometric data obtained from solutions of known pH: the program pHab. *Ann Chim* 89.
- [71] Cansu Ergun, E.G., Ertas, G., Eroglu, D., 2020. A benzimidazole-based turn-off fluorescent sensor for selective detection of mercury (II). *J Photochem Photobio A Chem* 394, 112469. <https://doi.org/10.1016/J.JPHOTOCHEM.2020.112469>.
- [72] Jiang, J., Lu, Y., Liu, J., Zhou, Y., Zhao, D., Li, C., 2020. An acid-base resistant Zn-based metal-organic framework as a luminescent sensor for mercury(II). *J Solid State Chem* 283, 121153. <https://doi.org/10.1016/J.JSSC.2019.121153>.
- [73] Bozkurt, E., Gul, H.I., 2020. Selective fluorometric “Turn-off” sensing for Hg<sup>2+</sup> with pyrazoline compound and its application in real water sample analysis. *Inorg Chim Acta* 502, 119288. <https://doi.org/10.1016/J.ICA.2019.119288>.
- [74] Bhardwaj, V., Nurichi, V.M., Sahoo, S.K., 2021. Mercury toxicity and detection using chromo-fluorogenic chemosensors. *Pharmaceuticals* 14, 1–45. <https://doi.org/10.3390/PH14020123>.
- [75] Kavitha, B.S., Sriveli, S., Makam, P., Ghosh, D., Govindaraju, T., S. A., et al., 2021. Highly sensitive and Rapid detection of mercury in water using functionalized etched fiber Bragg grating sensors. *Sens Actuators B Chem* 333, 129550. <https://doi.org/10.1016/J.SN.2021.129550>.
- [76] Galhano, J., Marcelo, G.A., Duarte, M.P., Oliveira, E., 2022. Ofloxacin@ Doxorubicin-Epirubicin functionalized MCM-41 mesoporous silica-based nanocarriers as synergistic drug delivery tools for cancer related bacterial infections. *Bioorg Chem* 118, 105470. <https://doi.org/10.1016/j.bioorg.2021.105470>.
- [77] Gong, H.-H., Addla, D., Lv, J.-S., Zhou, C.-H., 2016. Heterocyclic naphthalimides as new skeleton structure of compounds with increasingly expanding relational medicinal applications. *Curr Top Med Chem* 16, 3303–3364. <https://doi.org/10.2174/1568026616666160506145943>.
- [78] Dai, F., Li, Q., Wang, Y., Ge, C., Feng, C., Xie, S., et al., 2017. Design, synthesis, and biological evaluation of mitochondrial-targeted flavone–naphthalimide–polyamine conjugates with antimetastatic activity. *J Med Chem* 60, 2071–2083. <https://doi.org/10.1021/acs.jmedchem.6b01846>.
- [79] Chen, Y.-Y., Gopala, L., Bheemanaboina, R.R.Y., Liu, H.-B., Cheng, Y., Geng, R.-X., et al., 2017. Novel naphthalimide aminothiazoles as potential multitargeting antimicrobial agents. *ACS Med Chem Lett* 8, 1331–1335. <https://doi.org/10.1021/acsmmedchemlett.7b00452>.
- [80] Delcour, A.H., 2009. Outer membrane permeability and antibiotic resistance. *Biochim Et Biophys Acta (BBA) - Proteins Proteom* 1794, 808–816. <https://doi.org/10.1016/j.bbapap.2008.11.005>.
- [81] Blair, J.M., Richmond, G.E., Piddock, L.J., 2014. Multidrug efflux pumps in Gram-negative bacteria and their role in antibiotic resistance. *Future Microbiol* 9, 1165–1177. <https://doi.org/10.2217/fmb.14.66>.
- [82] Hernández-Fernández, F.J., Bayo, J., Pérez de los Ríos, A., Vicente, M.A., Bernal, F. J., Quesada-Medina, J., 2015. Discovering less toxic ionic liquids by using the Microtox® toxicity test. *Ecotoxicol Environ Saf* 116, 29–33. <https://doi.org/10.1016/j.ecoenv.2015.02.034>.
- [83] Alba, P., Sánchez-Forcín, S., Alvarez-Perez, S., Blanco, J.L., García, M.E., 2009. Use of a microbial toxicity test (Microtox®) to determine the toxicogenicity of *Aspergillus fumigatus* strains isolated from different sources. *Toxicol* 53, 729–733. <https://doi.org/10.1016/j.toxicon.2009.02.009>.
- [84] de García, S.O., García-Encina, P.A., Irusta-Mata, R., 2016. Dose-response behavior of the bacterium *Vibrio fischeri* exposed to pharmaceuticals and personal care

- products. Ecotoxicology 25, 141–162. <https://doi.org/10.1007/s10646-015-1576-8>.
- [85] Domínguez, C.M., Ventura, P., Checa-Fernández, A., Santos, A., 2023. Comprehensive study of acute toxicity using Microtox® bioassay in soils contaminated by lindane wastes. Sci Total Environ 856, 159146. <https://doi.org/10.1016/j.scitotenv.2022.159146>.
- [86] Halmi, M.I.E., Jirangon, H., Johari, W.L.W., Abdul Rachman, A.R., Shukor, M.Y., Syed, M.A., 2014. Comparison of microtox and xenoassay light as a near real time river monitoring assay for heavy metals. Sci World J 1–10. <https://doi.org/10.1155/2014/834202>.